Topical Review

In situ and *operando* Raman spectroscopy of semiconducting photoelectrodes and devices for photoelectrochemistry

Marco Favaro[1,*] , **Heejung Kong**[1] **and Ronen Gottesman**[2,*]

[1] Institute for Solar Fuels, Helmholtz-Zentrum Berlin für Materialien und Energie GmbH, Hahn-Meitner-Platz 1, 14109 Berlin, Germany
[2] Institute of Chemistry and The Center for Nanoscience and Nanotechnology, The Hebrew University of Jerusalem, Jerusalem 9190401, Israel

E-mail: marco.favaro@helmholtz-berlin.de and ronen.gottesman@mail.huji.ac.il

CrossMark

Abstract

Future alternative and promising energy sources involve photoelectrochemical (PEC) devices that can convert sunlight and abundant resources such as water and CO_2 into chemical fuels and value-added products. However, identifying suitable photoabsorber semiconductor materials that fulfill all the stringent requirements of photoelectrodes in PEC devices remains a significant challenge. A key factor for tailoring and optimizing existing and novel photoabsorbers is understanding the processes occurring at the semiconductor/liquid electrolyte interface under working conditions. This perspective focuses on the application of *operando* Raman spectroscopy (RS) in synergy with (photo)electrochemical techniques. Despite being a relatively new field of application, when applied to photoelectrochemistry, *operando* RS offers insights into the evolution of photoelectrode structure (i.e. phase purity and degree of crystallinity) and surface defects under working conditions. The challenges associated with *operando* RS for (photo)electrochemical applications, including the low quantum efficiency of inelastic scattering and fluorescence, and possible mitigation strategies are discussed. Furthermore, practical aspects such as sample/reactor geometry requirements and the surrounding environment of the photoelectrode sample during *operando* RS under PEC conditions are reviewed. We demonstrate that *operando* RS can be used to perform product analysis of solar-driven biomass reforming reactions, showing the approach's limitations and discussing possible solutions to overcome them. This work concludes with a discussion on the current state of *operando* RS of semiconducting photoelectrodes and devices for

---

* Authors to whom any correspondence should be addressed.

J. Phys. D: Appl. Phys. **57** (2024) 103002

Topical Review

photoelectrochemistry. We show a new methodology for performing *operando* RS with illumination resembling *AM*1.5 conditions and with time resolution spanning from tens to hundreds of milliseconds, suitable timescales for real-time monitoring of chemical reactions and degradation mechanisms occurring at the photoelectrode under investigation.

1. Introduction

The world's growing energy demands call for increased renewable energy sources. Photoelectrochemical (PEC) conversion of cheap, abundant resources, such as water and CO_2, into chemical fuels and value-added products is a highly sought-after goal in renewable energy production [1–5]. However, identifying suitable light-absorbing semiconductors for constructing photoelectrodes is a major challenge that has yet to be solved. Despite 50 years of research [6], the requirements for practical deployment of PEC devices are not yet fulfilled by a single semiconducting photoabsorber, contrary to the tremendous technological progress of solid-state photovoltaic devices [7–11]. However, the growing rate of photoelectrode materials discovery through new synthesis pathways or compositional exploration, often accelerated by high-throughput experimentation and machine learning, is highly encouraging. New compounds with the desired properties will likely be found within vastly unexplored synthesis and composition spaces, encompassing different material classes (e.g. oxides, nitrides, chalcogenides, heteroanionic compounds) [12–16]. Regardless of their synthesis and structural nature [17, 18], new approaches to material characterization under realistic working conditions are necessary to gain in-depth information while remaining up to speed with the accelerated materials discovery.

A rational multimodal approach is needed to achieve a molecular-level understanding of how photoelectrodes work under true PEC conditions (i.e. *AM*1.5 illumination). Here, we focus on *operando* Raman spectroscopy (RS), which can be used in synergy with x-ray spectroscopies and (photo)electrochemical techniques to correlate the nature and energetics of the electronic states at the solid/liquid interface with the degree of crystallinity/phase purity of the investigate photoelectrodes. Comprehending such a complex interplay can shed new light on the causes of photovoltage losses and charge carrier dynamics in the material's bulk and at interfaces. These factors steer the PEC performance and stability of semiconducting photoelectrodes [16, 19–21].

RS has made significant progress over the last four decades, with a reawakening in 1986 owing to Fourier transform RS [22] and the introduction of technological developments such as charge-coupled detectors (CCD), highly-performing computers, and near-infrared (NIR) lasers that overcame major impediments in that era [23]. Since then, the synergism of these technologies and the ability to locally guide and collect the excitation light and Raman signal using fiber optics has stimulated renewed interest in the technique, making it a valuable material characterization and analysis tool with applications in many fields of fundamental and applied research.

A particular strength of RS relies on its adaptability to different experimental configurations, from compact handheld instruments to high-resolution multistage lab systems. This non-destructive vibrational spectroscopy can be applied to samples in solid, liquid, or gas phases at various temperatures and pressures and requires little to no sample preparation [24–32]. Additionally, RS can be applied to both organic and inorganic compounds, making it a versatile tool for product analysis across different fields of application.

Due to its high versatility, RS can provide molecular-level information about the evolution of the physical/chemical properties of materials undergoing a chemical reaction or other processes under controlled *operando* methodology conditions [33–35], i.e. within reaction environments, allowing real-time monitoring of dynamic processes without disturbing the system. Depending on the particular experimental conditions, RS allows to detect and analyze transient changes occurring within a few ms (*vide infra*) [36], thereby matching the typical timescale of ionic rearrangement at the electrified solid/liquid interface and redox reactions [37]. Additionally, RS can be employed to analyze reaction products under working conditions since it enables the identification of chemical species present in the sample environment. Each chemical compound exhibits a unique Raman spectrum, which serves as a molecular fingerprint. The presence and identity of specific compounds can be determined by comparing the obtained Raman spectrum to reference spectra in databases or known standards. By correlating the intensity of Raman bands with the concentration of a specific component, it is possible to determine the amount or percentage of that component in a mixture. This quantitative analysis can be achieved by employing calibration curves or multivariate analysis techniques such as chemometrics. Moreover, RS can monitor real-time chemical or (photo)redox reactions. By continuously acquiring Raman spectra during a reaction, it is possible to track changes in molecular structure and composition, identify reaction intermediates and products, and study reaction kinetics, helping understand reaction mechanisms and optimize reaction conditions [38]. However, it is essential to highlight that the Raman signal is characterized by a weaker intensity concerning other competitive processes (e.g. Rayleigh scattering, fluorescence, and photoluminescence (PL)) [39]. This requires caution when using RS for liquid product analysis of solar-driven reactions, where

J. Phys. D: Appl. Phys. **57** (2024) 103002

Topical Review

the low signals and eventual spectral overlaps can hinder the investigation. Hence, a case-by-case analysis must be performed, considering the given experimental conditions and the scattering power of the molecules involved. This perspective will also provide possible mitigation strategies that can be applied to amplify the intensity of the Raman signal.

From the view of (photo)electrochemical applications, vibrational techniques such as Raman and Fourier transform infrared (FTIR) spectroscopies [40–52] cover a wide range of wavelengths, allowing the investigation of different energy scales and vibrational modes in both semiconducting photoelectrodes and liquid electrolytes. However, RS offers some advantages over FTIR when performed under *operando* conditions due to several reasons: (i) RS can investigate samples immersed in aqueous solution due to the weak active Raman modes of water molecules; (ii) RS is capable of performing noninvasive temperature measurements; (iii) RS is not sensitive to blackbody radiation, allowing for measurements at high temperatures; (iv) using specialized RS configurations (e.g. confocal Raman microscope), slices of well-defined volumes of the samples at different distances from the surface can be measured; (v) Molecules such as O_2 or H_2, products of water splitting, are Raman active and, therefore, can be detected using Raman (albeit high-concentration is required, *vide infra*).

Photoelectrodes differ from particulate photocatalysts by having a photocatalytic semiconducting thin film (with or without a co-catalyst on its surface) deposited on a transparent conductive substrate. The alignment between the energy levels of the semiconductor thin film and the substrate's work function is required to allow the contact selectivity for a particular charge carrier (electrons or holes) and the consequent charge transfer [53]. Using *operando* RS of semiconducting photoelectrodes and devices for photoelectrochemistry, in synergism with other x-ray spectroscopies and (photo)electrochemical techniques, can give valuable information essential in studying new materials under different working conditions. In particular, information such as the formation of passivation layers, transient structural/chemical changes, lattice distortions, and differentiation of polymorphs can be gained, enabling the understanding of the influence of different synthesis pathways. *Operando* RS thus allows correlating this set of information with the PEC performance and stability of the investigated systems. On the other hand, *operando* RS is scarcely used in the study of semiconducting photoelectrodes and devices for photoelectrochemistry. To the best of our knowledge, only one report of semiconducting photoelectrodes and devices for photoelectrochemistry using *in situ* and *operando* RS exists. Recently, Ramakrishnan *et al* reported a competitive photo-oxidation of water and hole scavengers on hematite photoelectrodes using *operando* RS [54]. A similar approach was conducted in studying a PEC dye-sensitized solar cell, directly detecting charge transfer processes [55]. Given its relatively straightforward and inexpensive nature, *operando* RS is highly regarded as a valuable research tool. Its utilization in multimodal approaches is crucial for attaining a molecular-level understanding of PEC processes.

Furthermore, an additional incentive for implementing RS in *operando* experiments is represented by the growing use of machine learning techniques to decode Raman data and contribute to expanding the existing spectral databases [56, 57].

In this perspective, we focus on using *operando* RS in studying semiconducting photoelectrodes and devices for photoelectrochemistry and its coupling with complementary characterization tools based on UV–VIS and x-ray spectroscopies. Despite the great potential held by *operando* RS, its application has been hindered by the low quantum efficiency of the Raman scattering process and the occasional occurrence of fluorescence and PL that overshadow the Raman signal. In the following sections, we discuss these challenges and others related to (photo)electrochemical applications and approaches to overcome them. The perspective is divided into seven sections: (1) etymology of the terms '*in situ*' and '*operando*', (2) principles and theory of RS, (3) challenges of RS and mitigation strategies, (4) challenges of *operando* RS for the characterization of semiconducting photoelectrodes and devices for photoelectrochemistry, (5) geometry around the sample and sample environment for *operando* RS, (6) state of the art of *operando* RS of semiconducting photoelectrodes and devices for photoelectrochemistry, (7) conclusions and future perspectives.

2. Etymology of the terms '*in situ*' and '*operando*'

In this section, we want to clarify the etymology of the terms '*in situ*' and '*operando*', as they are used and meant throughout this perspective. *Operando* spectroscopy expresses a methodology that combines *in situ* spectroscopy with simultaneous kinetic measurements/product analysis carried out on the sample and its environment during working conditions. We emphasize that '*operando*' (literally working, operating) means an action, whereas '*in situ*' means 'at a location,' and etymologically, the term has no temporal insights. An '*operando*' methodology describes an '*in situ*' spectroscopic investigation performed under actual (photo)catalytic operations. Hence, the term '*operando*' provides a single word that underlines the simultaneous evaluation of both chemical composition/structure (active catalytic sites/phases and surface reaction intermediates) and (photo)catalytic activity/selectivity. Within this definition, note that the term '*in situ*' itself can describe different types of studies. For instance:

a) The spectroscopic investigation of a (photo)catalytic sample in the same environment where it has been pretreated or activated.
b) The monitoring of the physical/chemical transformations of the photocatalyst or photoelectrode occurring with respect to an experimental variable, such as time, temperature, applied potential, light intensity, etc.
c) The spectroscopic investigation of a (photo)catalytic sample carried out under reaction conditions relevant to the (photo)catalytic operation without the simultaneous evaluation of the reaction kinetics and products.
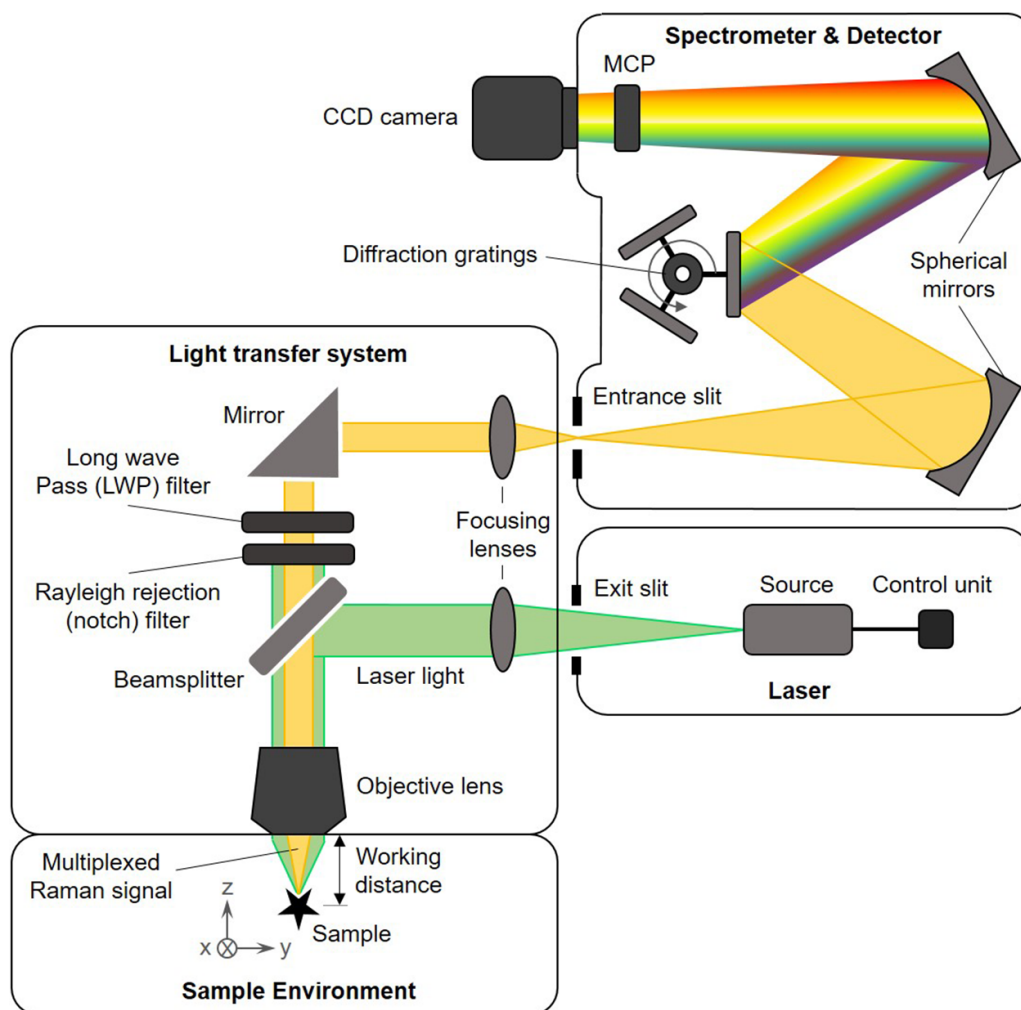
J. Phys. D: Appl. Phys. **57** (2024) 103002

Topical Review

Figure 1. Schematic diagram of an RS measurement setup in backscattering configuration showing the general working principle. Note that different experimental configurations are possible, especially in the light transfer system; see the text for more details. CCD: charge-coupled device; MCP: multichannel plate.

3. Principles and theory of RS

In this section, we will outline some basic introductory principles of RS. We refer readers to excellent sources [58, 59] for an in-depth analysis of the theoretical aspect of this technique.

Raman spectroscopy (named after Chandrasekhara Venkata Raman, Nobel laureate in 1930) [60, 61] measures and analyzes the inelastic (or Raman) scattering of monochromatic laser light when guided through a sample. As schematically shown in figure 1, a typical RS setup is constituted of four main parts: the sample and its surroundings (positioning system, environment), the excitation laser source, the spectrometer and detector (for light analysis and detection), and the transfer system that guides the light from the laser source to the sample and from the sample to the spectrometer. This part is available in different experimental configurations, depending on the particular application and targeted versatility of the Raman instrument. It spans from confocal systems implemented on optical microscopes to fiber-coupled setups where the laser source and spectrometer are encased in the same volume, and the production of the excitation light and the detection of the scattered

radiation are carried out without any moving part. Note that the working principle of an RS setup shown in figure 1 is general and applies to all possible experimental configurations.

The typical wavelengths of lasers used to induce and detect the Raman scattering range from NIR and visible to near-ultraviolet radiation (NIR-UV, e.g. $\lambda = 1064$–248 nm, corresponding to an energy range of about 1.2–5 eV). The laser light interacts with bond or lattice vibrations in the investigated material, resulting in an upward or downward energy shift of the laser light. The energy shift (usually measured in cm^{-1}, 1 eV–8065.61 cm^{-1}) depends on the sample response to the incident laser and not on the wavelength of the excitation light. The collected spectrum provides a 'chemical fingerprint' of the vibrations or other excitations in the sample, allowing the identification of the chemical compounds and their structural characteristics (for instance, RS enables the differentiation of different isomers and polymorphs). RS gives information about the sample's low-frequency (short-range) and collective vibrational modes (long-range) characteristics. Therefore, it can also be used to analyze amorphous materials, gasses, and liquids. Experimental setups allowing to detect Raman shift

between a few tens and about 1500 cm^{-1} provide the necessary flexibility to investigate lattice vibrations (e.g. acoustic and optical phonons) and molecular modes, thereby enabling the possibility to investigate both semiconducting photoelectrodes and liquid electrolytes used in the PEC devices. Systems covering extended ranges of Raman shift, up to 4000 cm^{-1}, offer the highest detection flexibility, as documented by table 1. Noteworthy, standard low-resolution spectrometers in many chemistry laboratories allow detecting Raman shifts starting from 250–300 cm^{-1} from the excitation line, equivalent to energy shifts of about 30–40 meV. However, inorganic materials, mainly transition metal oxides as reported in table 1, possess Raman modes characterized by wavenumbers below 200 cm^{-1} within the so-called Tera Hertz (THz) Raman region (note that the investigation of long-range, low energy (acoustic) lattice vibrations is also known as Brillouin scattering). Such energy region is extremely valuable for identifying polymorphic forms and quantifying the degree of crystallinity of the material. Hence, a thorough characterization of photocatalysts and photoelectrodes based on transition metal oxides requires optical configurations capable of detecting RS at such low energy shifts.

RS uses a single frequency of radiation to irradiate the sample, and the multiplexed radiation scattered from the sample is detected. Thus, unlike infrared absorption, RS does not require matching the incident radiation to the energy difference between the ground and excited states of the studied materials, although this might be useful to increase the signal's intensity (see next section). Consequently, in solid materials, the sample's microstructure and morphology change the system's response to the incident light, enabling RS to detect subtle synthesis-dependent structural changes.

NIR and UV–VIS radiation interact with matter through absorption and/or scattering. An absorption process requires matching the incident photon's energy with the energy gap between the two electronic energy levels. On the contrary, the scattering process does not require suitable energy levels, as it occurs when a photon interacts with a crystal lattice or a molecule, inducing a distortion of its electron cloud and changing the species' polarization by involving a so-called 'virtual state' (see figure 2). This is an electronic transition from the electronic ground state to an intermediate electron-hole pair state, taking place with the annihilation of the incident photon. For this reason, virtual states are not necessarily true quantum states of the material. They are short-lived and characterized by a rapid decay, leaving the electron in the initial electronic level of the system while a photon is emitted as a response to the virtual/ground state 'transition'. Note that the energy is thus conserved only in the total process. Two types of scattering events can occur:

1. The photon is elastically scattered (Rayleigh scattering). This event has the highest probability and occurs when the energy of the scattered photon matches the incoming one, and the electron involved returns to a state with the same energy as the initial one (e.g. from level V_1 to a virtual state, and then returns to the V_1 level).

2. The photon is inelastically scattered (Raman scattering). During inelastic scattering, the photon energy loss or gain equals the energy difference between the initial and final vibrational levels of the ground electronic state. The energy difference (ΔV) between the incoming and emitted photon is called the 'Raman shift.' If the scattered photon has a lower energy than the incoming one, the process is called Raman Stokes scattering. If the scattered photon has a higher energy than the incoming one, the process is called Raman Anti-Stokes scattering. Typically, at room temperature, Stokes scattering would have a higher intensity than anti-Stokes because of the much lower population of $V_{2 \to n}$ levels than the lowest V_1 level.

RS can be employed for chemical recognition since it identifies chemical species in the sample and sample environment. Each chemical compound exhibits a unique Raman spectrum, which serves as a molecular fingerprint. The presence and identity of specific compounds can be determined by comparing the obtained Raman spectrum to reference spectra in databases or known standards. Moreover, RS can be used to quantify the presence of the different chemical species. By correlating the intensity of Raman bands with the concentration of a specific component, it is possible to determine the amount or percentage of that component in a mixture. This quantitative analysis can be achieved by employing calibration curves of samples with known concentrations or multivariate analysis techniques such as chemometrics.

Raman scattering is inherently a low-yield process, where only one in every 10^6–10^8 scattered photons is inelastically scattered. This does not make the process insensitive because modern lasers and microscopes can deliver high-power densities to small sample volumes. However, other processes, such as sample degradation and fluorescence, can readily occur. In the next section, these challenges are discussed, and possible mitigation strategies are presented.

4. Challenges of RS and mitigation strategies

RS is characterized by two main challenges: (i) occasionally occurring fluorescence, which can overlap with Raman spectral features, and (ii) relatively low sensitivity. The detection sensitivity of the spontaneous Raman signal can be increased, and the background fluorescence can be avoided (or minimized), by using different approaches. The Raman signal-enhancing mechanisms can be discussed by considering the factors that determine the intensity of the Stokes–Raman scattered light, I_{Stokes}, given in equation (1):

$$I_{\text{stokes}} \propto I_0 \left(\omega - \omega_{0,q}\right)^4 | \alpha |^2 \tag{1}$$

where I_0 is the incident light intensity with frequency ν ($\omega = 2\pi\nu$), $\omega_{0,q}$ is the vibrational frequency, and α is the system's polarizability that determines the response of the electron cloud to the electric field of the incident laser light. The scattering intensity can increase at shorter wavelengths due to its fourth power proportionality to the frequency of the

J. Phys. D: Appl. Phys. **57** (2024) 103002

Topical Review

Table 1. Wavenumbers of vibrations for common organic molecular functional groups and transition metal oxides at room temperature (25 °C). Note that the values reported in the table can vary based on sample preparation, environmental conditions, and material form (powders, thin films, single crystals, nanostructures etc.). Sources: (a) Smith and Dent [58]; (b) Senthilkumar *et al* [62]; (c) Szatkowski *et al* [63]; (d) Tsay *et al* [64]; (e) Davies [65].

Lattice vibrations (phonons)[a]
- Acustic modes: 0–300 cm^{-1}
- Optical modes: 300–1500 cm^{-1}

Molecular vibrations (Organic Compounds)[a]
- C–C stretching (ring breathing): 1000–1600 cm^{-1}
- C–C stretching (aliphatic): 1000–1600 cm^{-1}
- C–H stretching: 2800–3100 cm^{-1}
- C–H bending: 1000–1600 cm^{-1}
- C–O stretching: 900–1800 cm^{-1}
- C=O stretching: 1600–1800 cm^{-1}
- N–H stretching: 3100–3500 cm^{-1}
- O–H stretching: 3000–3800 cm^{-1}

Inorganic vibrations (Inorganic Compounds)[a]
- Metal-O stretching: 400–900 cm^{-1}
- Metal-O bending: 400–800 cm^{-1}
- Metal-N stretching: 300–700 cm^{-1}

Polymers and other carbon-based materials[a]
- CH2 wagging and twisting modes: 1200–1400 cm^{-1}
- CH2 symmetric and asymmetric stretching: 2800–3000 cm^{-1}
- C–C and C=C stretching: 1600–1700 cm^{-1}
- Graphitic carbon nitride (g-C_3N_4): 1200–1300 cm^{-1}
- Graphene, G band (in-plane vibrational modes): 1550–1600 cm^{-1}
- Graphene, D band (disordered or defect-induced modes): 1300–1400 cm^{-1}
- Graphene, 2D band (second-order mode): 2600–2700 cm^{-1}
- Carbon nanotubes, radial breathing modes (RBM): 100–300 cm^{-1}
- Carbon nanotubes, tangential modes (G band): 1550–1600 cm^{-1}
- Carbon nanotubes, disordered modes (D band): 1300–1400 cm^{-1}

Oxide semiconducting photoabsorbers

Rutile TiO_2 (*n*-type, $E_g \sim 3.0$ eV)[a]
B_{1g} mode (symmetric stretching): 142–144 cm^{-1}
Multi-photon process: 235–245 cm^{-1}
E_g mode (symmetric stretching): 443–448 cm^{-1}
A_{1g} mode (symmetric bending): 610–615 cm^{-1}
B_{2g} mode (antisymmetric bending): 825–835 cm^{-1}

Anatase TiO_2 (*n*-type, $E_g \sim 3.2$ eV)[a]
E_g mode (symmetric stretching): 145–155 cm^{-1}
E_g mode (antisymmetric stretching): 194–202 cm^{-1}
B_{1g} mode (symmetric stretching): 395–405 cm^{-1}
A_{1g}, B_{1g} mode (symmetric bending): 515–525 cm^{-1}
E_g mode (antisymmetric bending): 635–645 cm^{-1}

Tungsten trioxide (WO_3) (*n*-type, $E_g \sim 2.7$ eV)[b]
O–W–O bending: 290–295 cm^{-1}
O–W–O bending: 344–350 cm^{-1}
O–W–O stretching: 715–720 cm^{-1}
O–W–O stretching: 805–810 cm^{-1}

Hematite (α-Fe_2O_3) (*n*-type, $E_g \sim 2.2$ eV)[c]
A_{1g} mode: 225–230 cm^{-1}
E_g mode: 242–248 cm^{-1}
E_g mode: 290–295 cm^{-1}
E_g mode: 297–300 cm^{-1}

(Continued.)

Table 1. (Continued.)

E_g mode: 410–415 cm^{-1}
A_{1g} mode: 495–500 cm^{-1}
E_g mode: 610–615 cm^{-1}

Bismuth vanadate (BiVO$_4$) (n-type, $E_g \sim 2.4$ eV)^d
External mode (1): 120–125 cm^{-1}
External mode (2): 205–210 cm^{-1}
$\delta(VO)_4^{3-}$(antisymmetric stretching): 320–325 cm^{-1}
$\delta(VO)_4^{3-}$(symmetric stretching): 360–365 cm^{-1}
ν_{as}(V–O) (A_g mode, V–O antisymmetric stretching): 710–715 cm^{-1}
ν_s(V–O) (A_g mode, V–O symmetric stretching): 820–825 cm^{-1}

Bismuth oxyiodide (BiOI) (p-type, $E_g \sim 1.9$ eV)^e
A_{1g} mode (symmetric stretching): 82–87 cm^{-1}
E_g mode (antisymmetric stretching): 150–155 cm^{-1}
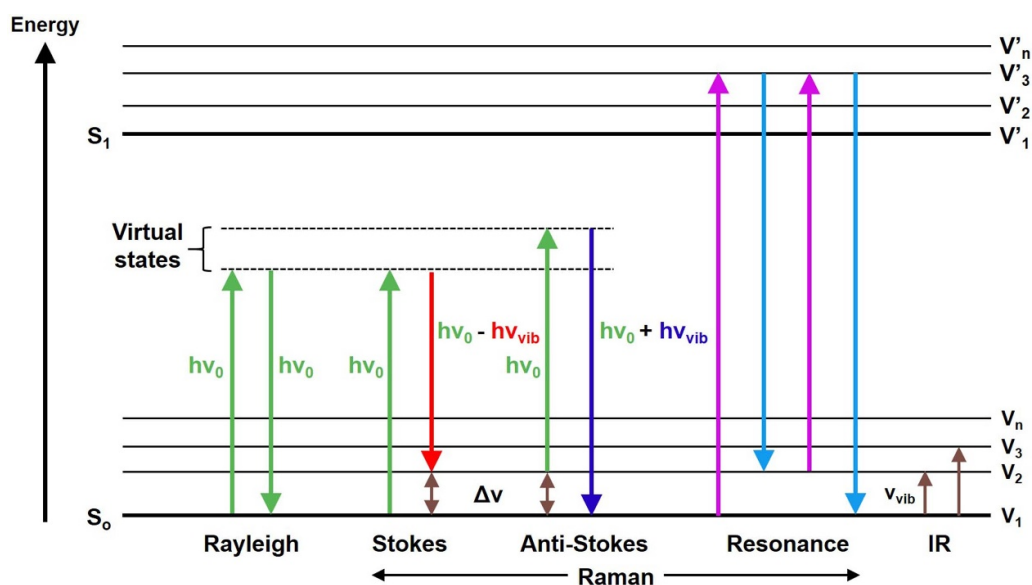B_{1g} mode (symmetric bending): 338–342 cm^{-1}

Figure 2. Energy diagram showing the transitions during Rayleigh, Raman Stokes, anti-Stokes, and resonance Raman scattering. The transition during IR absorption is shown for comparison purposes. Vibrational states (V_n) in the ground electronic state (S_0) can be probed by directly measuring the Raman shift (Stokes and anti-Stokes) of the allowed transitions. Resonance Raman also involves the vibrational states (V'_n) of the excited electronic state (S_1). $h\nu_0$ = incident laser energy, $h\nu_{vib}$ = vibrational energy, $\Delta\nu$ = Raman shift, and ν_{vib} = vibrational frequencies. Reproduced from [66]. CC BY 4.0.

incident laser light. Equation (1) also shows that the Stokes–Raman intensity can be enhanced by increasing either α or I_0. The polarizability α can be efficiently increased, and therefore, the overall Stokes intensity, using the most common enhancement technique, resonance Raman scattering (see figure 2). During resonant RS, the excitation wavelength of the incident light is tuned to match the electronic transition energy of the sample of interest (e.g. from V_1 to V'_1). Matching the excitation wavelength to an electronic transition from the electronic ground to an excited state enhances the Raman scattering process by increasing the system's polarizability, hence leading to higher-intensity Raman signals (in quantum mechanics' terms); the resonant excitation photon is efficiently absorbed by the system with a probability, or cross-section, higher than a non-resonant photon, resulting in increased Raman

scattering). The exact magnitude of the intensity enhancement in resonant RS can vary significantly depending on the specific material and the details of the experimental setup. In some cases, resonance Raman signals can be several orders of magnitude stronger than non-resonance Raman signals, enabling the detection of weak Raman signals even in the presence of fluorescence. Surface-enhanced Raman scattering (SERS) can also be used to increase the detection sensitivity by the local increase of I_0, regarding equation (1). SERS is a technique that utilizes nanostructured metal surfaces (such as silver or gold) to enhance the Raman signal. The incident laser light induces the formation of synchronous plasmons (i.e. collective oscillations of free electrons) within the metal nanostructures, thereby amplifying the electric field. When the sample is near the metal surface, the amplified electric field around the metal

J. Phys. D: Appl. Phys. **57** (2024) 103002

Topical Review

nanostructures can enhance the Raman scattering signal by several orders of magnitude [67]. SERS improves the sensitivity and reduces the influence of background fluorescence, as the enhancement mechanism selectively enhances the Raman signal rather than the fluorescence emission [68, 69]. Another experimental solution to increase the technique's sensitivity by suppressing fluorescence is known as time-gated RS [70]. [REF] This technique involves delaying the detection of the Raman signal relative to the excitation pulse, taking advantage of the differences in the fluorescence and Raman lifetimes (inelastic scattering timescales being faster than fluorescence or PL de-excitation mechanisms). By employing a time-delayed gate window, the fluorescence emission can be temporally separated from the Raman signal, allowing for the selective detection of the Raman scattering and minimizing the fluorescence background. Carefully selecting the excitation wavelength can also help minimize fluorescence interference. This can be achieved by choosing an excitation wavelength corresponding to a region where the typical samples under investigation exhibit minimal or negligible fluorescence. Using NIR excitations can help alleviate the fluorescence interference since the frequency (energy) is too low to excite fluorescence [43]. However, despite using high-power lasers, NIR light may not be sufficient to attain reasonable Raman scattering in the case of very diluted samples or molecules with low scattering powers (i.e. scattering cross section). An enhancement in sensitivity can be achieved by using high laser fluencies. However, great care has to be taken to avoid sample damage, ranging from an increase in the sample's temperature and structural modification to its degradation. Typical approaches to avoid damage when investigating solid samples rely on periodically moving the position of the laser spot on the sample and decreasing the data acquisition time while maintaining an acceptable signal-to-noise ratio.

Finally, a separate discussion must be conducted for the qualitative and quantitative analysis of liquid reaction products using RS. In the literature, many excellent examples are reported on chemical analysis of liquid reaction environments performed using RS [39, 71–75]. These studies predominantly deal with relatively concentrated solutions and products, with concentrations up to hundreds of mmoles l^{-1} [39]. However, a limitation of PEC reactions is the relatively low current densities generated by the process. Figure 3(a) shows a transient (light on/light off) j–V curve obtained from a polycrystalline, un-doped $BiVO_4$ sample prepared by electrodeposition [76], in contact with an aqueous electrolyte (pH 2) containing 0.5 M $NaNO_3$, with glycerol (0.5 M) as a hole scavenger/electron donor (green curve) and without glycerol (dark curve). Solar-driven biomass reforming offers a potential solution to replace the sluggish oxygen evolution reaction at photoanode with the more favorable organic molecule oxidation due to lower kinetic overpotentials and increased contact selectivity for minority carriers (i.e. holes) [77–79]. The data were obtained using the flow cell described in detail in the 'State of the art of *operando* RS of semiconducting photoelectrodes and devices for photoelectrochemistry' section at a flow rate of 10 ml min^{-1}.

It is noticeable that the addition of glycerol decreases the onset of the anodic potential and increases the photocurrent and the overall fill factor due to the drastic reduction of the kinetic overpotentials required to oxidize glycerol compared to water [77–79] and for the increased extraction rate of holes, respectively. This is well-documented by fixing the electrode potential (ΔE_{WE-RE}) at +1.23 V vs. RHE for both solutions. Without glycerol, the photocurrent and the cell voltage (ΔE_{WE-CE}) were equal to about 1.1 mA cm^{-2} and 2.07 V, respectively. For the electrolyte containing instead 0.5 M of glycerol, the photocurrent and the cell voltage were equal to about 3.2 mA cm^{-2} and 1.72 V, respectively, with a net gain of about 290% in terms of photocurrent and 350 mV in the overall cell voltage. In figure 3(b), a simplified schematic of the reaction mechanism of glycerol oxidation is provided, highlighting the two major products, glyceric acid (GA) and dihydroxyacetone (DHA) [80, 81]. The liquid stream leaving the PEC cell was analyzed with RS at the beginning and end of an electrolysis experiment performed at a fixed current density of 3.2 mA cm^{-2}. The two spectra and their spectral difference (i.e. the spectrum after 12 h of electrolysis—the spectrum at $t = 0$ h) are reported in figures 3(c) and (d), respectively. Note that the difference spectrum was obtained after normalizing the Raman spectra for the intensity of the NO_3^- band centered at about 1048 cm^{-1}. As shown in figure 3(d), the difference spectrum exhibits positive intensity, particularly at around 600 and 800 cm^{-1}. In this region, an overlap exists between the glycerol and the GA and DHA C-C stretching mode bands. Despite this overlap, observing a positive intensity for wavenumbers below 800 cm^{-1} (where pure glycerol does not exhibit a Raman signal) allows us to conclude that the oxidation reaction most likely generates both GA and DHA. However, it is important to recognize that in-depth chemical speciation and quantification are rather complex, given the spectral overlap between the reactant and the reaction products and their low concentrations. A simple calculation based on Faraday's law of electrolysis can be done to estimate an upper limit for the reaction yield. The total charge (Q) passed during the 12 h of electrolysis was approximately 213 C (given the photoelectrode area of 1.54 cm^2 and the constant current density of 3.2 mA cm^{-2}, the electrolysis current was about 4.93 mA). Assuming a 100% Faradaic efficiency toward DHA (one electron transfer), the number of moles of DHA ($n_{mol} = Q/vF$) produced during the electrolysis is approximately 2.2 mmol, with v being the number of electrons exchanged during the electron transfer (1 for the oxidation of glycerol to DHA) and F being the Faraday constant ($\sim$96 485.33 C mol^{-1}). Hence, depending on the electrolyte volumes used in the PEC device (typically ranging from tens to hundreds of mL), the concentration of products after a few hours of electrolysis could be up to some tens of mM (i.e. mmol l^{-1}) at most, making a quantitative analysis with RS not trivial. This also strongly depends on the scattering power of the molecules involved in the process, where very Raman-active organic substrates might facilitate the analysis, despite the relatively diluted concentrations. In addition, reliable quantifications of relatively diluted products can be performed using advanced analysis methods such as partial least squares (PLS), asymmetrically reweighted penalized least squares (arPLS), or indirect hard
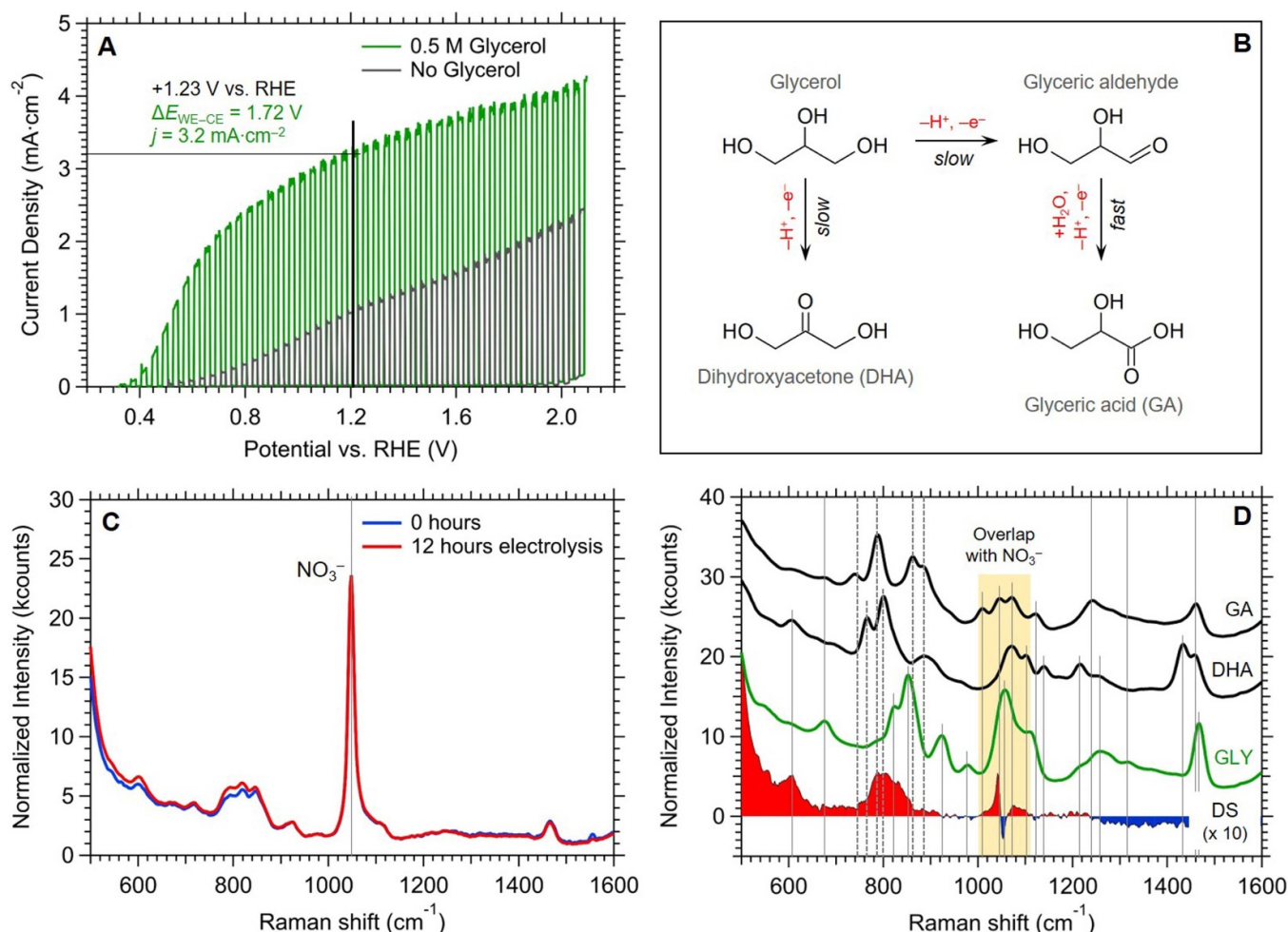
Figure 3. (A) Transient (light on/light off) j–V curve obtained from a polycrystalline, un-doped BiVO$_4$ sample prepared by electrodeposition on fluorine-doped tin oxide (FTO), in contact with an aqueous electrolyte (pH 2) containing 0.5 M NaNO$_3$, with glycerol (0.5 M) as a hole scavenger/electron donor (green curve) and without glycerol (grey curve). The flow rate was kept constant at 10 ml min^{-1}, while the scan rate and chopping frequency were equal to 20 mV s^{-1} and 0.5 Hz for both measurements. (B) Simplified schematic of the reaction mechanism of glycerol oxidation, highlighting the two major products, glyceric acid (GA) and dihydroxyacetone (DHA) (after [80, 81]). (C) Raman spectra of the electrolyte leaving the flow cell at the beginning of the electrolysis experiment (blue curve) and after 12 h of electrolysis at a constant current density of 3.2 mA cm^{-2} (red curve). The spectra are normalized for the intensity of the NO$_3^-$ band centered at a Raman shift of about 1048 cm^{-1}. (D) Difference spectrum (DS) (spectrum after 12 h of electrolysis—spectrum at $t = 0$ h) and spectral references (GLY: glycerol; DHA: dihydroxyacetone; GA: glyceric acid). The spectral references have been obtained from aqueous solutions of the abovementioned compounds at a concentration of 1.0 M. The reference spectra are normalized for the intensity of the water antisymmetric stretching mode centered at 1640 cm^{-1} and reported with a vertical offset.

modeling (IHM). A detailed description of these methods is beyond the scope of this perspective, and we refer readers to the [82–85] for the details of these analytical procedures. We also want to highlight the availability of excellent commercial software that allows performing the above analyses, for instance, PEAXACT [86], used in the authors' laboratories.

5. Challenges of *operando* RS for the characterization of semiconducting photoelectrodes and devices for photoelectrochemistry

Additional difficulties arise when a semiconducting photoelectrode is measured under PEC conditions (i.e. an aqueous solution, under a potential bias, and illuminated by a simulated 1 sun intensity). Semiconducting materials may undergo (photo)electrochemical corrosion due to underdeveloped synthesis pathways, non-optimized pH or local pH gradients at the semiconductor/liquid interface, and limited charge transfer kinetics, leading to the accumulation of charge carriers at the interface. It is known that different materials have faster reaction times than others under PEC conditions (i.e. Fe$_2$O$_3$ vs. BiVO$_4$). Therefore, to investigate such transient phenomena, time-resolved studies are needed, with the possibility to investigate the system in a wide range of time scales, from minutes/hours down to ms. This will help understand how (photo)electrochemical reactions occurring at the ms time scale are coupled to slower dynamics that, in turn, influence photoelectrodes' stability and long-term performance under

working conditions. However, RS typically operates at longer acquisition times, making capturing rapid changes in the system difficult. Specialized techniques, such as time-resolved RS, can overcome this challenge but may introduce additional complexity to the experimental setup.

A technical challenge of performing *in situ/operando* RS is coupling the broadband light source used to simulate 1-sun illumination with the Raman setup without saturating the detector. Different solutions can be used:

- For photocatalysis investigations, where relatively wide band gap ($\geqslant$2.5–3 eV) photoabsorbers are typically studied (e.g. TiO_2, ZnO, WO_3, $BiVO_4$) an excitation laser with wavelengths lower than $\sim$500 nm (corresponding to energies greater than $\sim$2.5 eV) can be used to induce the charge separation in the photocatalyst. The RS can be, therefore, performed using a higher wavelength laser (namely 532 nm, 633 nm, 785 nm, 830 nm, and 1064 nm), acquiring the Stokes lines and using a high-pass filter in front of the detector to eliminate the spectral component of the excitation laser ($\lambda \sim 500$ nm) from the multiplexed signal. The notch filter used to suppress the Rayleigh line might also serve that purpose, depending on the specifications of the particular optical analysis system. In general, careful consideration must be given to the choice of the laser wavelength and power used to perform RS on the photocatalyst/photoelectrode to avoid interfering with the sample's existing photoexcitation or causing unwanted photochemical reactions.
- PEC investigations involve photoelectrodes or tandem devices requiring an ample range of wavelengths to promote the charge separation in the material. Such investigations typically use broadband light sources (bias lights) that mimic the solar spectrum (e.g. *AM*1.5 irradiation conditions). Therefore, a spectral overlap between the frequencies contained in the bias light and the scattered laser light exists, thereby complicating the RS detection during illumination (known as 'background interference'). This background interference can mask or distort the Raman spectra, making it challenging to extract meaningful information. A possible technical solution to this challenge is outlined below in the section 'State of the art of *operando* RS of semiconducting photoelectrodes and devices for photoelectrochemistry.'

Additionally, it is important to remember that Raman signals are inherently weak; typically, one ppm of the overall photon flux directed to the sample undergoes inelastic scattering. *In situ/operando* conditions can further affect the signal-to-noise ratio of the measurements, for instance, due to the electrolyte's or bubbles' scattering during working operations. Achieving a good signal-to-noise ratio can be challenging, especially when dealing with low concentrations of analytes or studying subtle changes in the Raman spectra. Signal enhancement techniques, such as SERS or resonance Raman scattering, may be employed to improve sensitivity.

Despite these challenges, *in situ/operando* RS during PEC investigations provides valuable information about molecular vibrations, adsorbates, and structural changes occurring

at the electrode/electrolyte interface. With careful experimental design, optimization of measurement conditions, and appropriate data analysis techniques, meaningful insights can be obtained regarding the PEC processes and the structure/function relationships of the studied materials.

6. Geometry around the sample and sample environment for *operando* RS

Dedicated *in situ/operando* cells play a crucial role in photocatalysis and PEC studies by providing a controlled environment for studying the electrochemical and PEC processes occurring at the (electrified) semiconductor/liquid electrolyte interface. This section outlines why controlling the geometry around the sample and its surrounding environment is paramount, followed by the required experimental geometrical configurations to achieve that.

Reasons for controlling the geometry around the sample and its surrounding environment:

- Real-time analysis: *in situ/operando* cells/devices allow researchers to observe materials' electrochemical and PEC behavior in real-time. Researchers can monitor the material's performance under specific operating conditions by incorporating light sources and (photo)electrochemical measurement techniques, gaining valuable insights into charge transfer dynamics, reaction kinetics, and material degradation/photocorrosion.
- Environmental control: PEC processes are very susceptible to environmental factors such as temperature, humidity, and electrolyte/gas composition. Dedicated *in situ/operando* cells provide a controlled and tunable environment, allowing researchers to study materials under specific conditions relevant to practical applications. By varying parameters such as light intensity, temperature, or electrolyte/gas composition, researchers can investigate the impact of these factors on the performance and stability of photocatalysts and photoelectrodes.
- Long-term stability assessment: stability is crucial in developing PEC materials for practical applications. *In situ/operando* cells allow researchers to assess the stability of materials over extended periods. By subjecting the materials to continuous illumination and (photo)electrochemical cycling, it is possible to monitor their performance, degradation mechanisms, and overall durability changes. This information is essential for optimizing material compositions and designs to enhance stability.
- Device optimization: *in situ/operando* cells facilitate the optimization of PEC devices by providing a platform for systematic testing and characterization. Different material combinations, electrode architectures, and operating conditions can be screened and evaluated in a controlled manner. This iterative process helps identify the most efficient and stable configurations, leading to the development of high-performance and stable PEC devices.

Below we describe several key characteristics of the required experimental and geometrical configuration of PEC devices
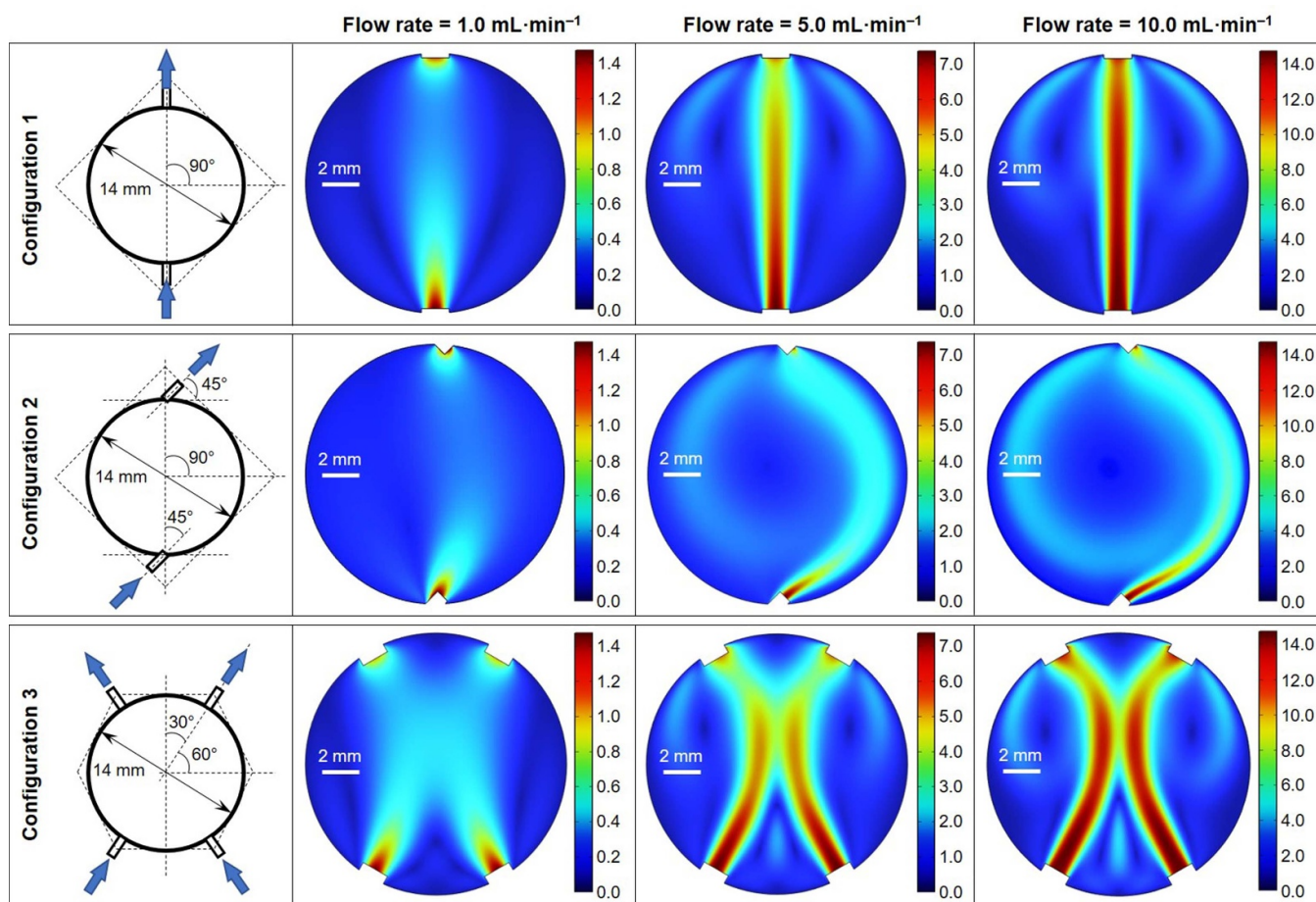
Figure 4. Fluid dynamics of three different electrolyte inlet/outlet configurations investigated with finite element analysis for three flow rates (1, 5, 10 ml min^{-1}). Configuration 2 provides a better flow homogeneity with respect to configurations 1 and 3 and was therefore selected for the geometry of the PEC flow cell described below. Note that the color bars report the velocity of the fluid in cm·s^{-1} and that the simulation of the velocity fields was performed for stationary flow conditions. Inlets and outlets have a diameter of 1.6 mm.

to ensure reliable and accurate results in the investigation of photoelectrodes under working conditions:

- Controlled flow: the electrolyte flow through the PEC cell should be well-controlled. This allows for uniform distribution of reactants and efficient mass transport to and from the photoelectrode surface and stable operation [87, 88]. The flow rate should be optimized to ensure an adequate supply of reactants to the photoelectrode surface while minimizing undesired side reactions and depletion effects. Additionally, the flow rate should be optimized to efficiently remove gas bubbles from the photoelectrode surfaces to minimize the optical losses due to the gas evolution and accumulation of bubbles at the electrodes [89]. Simulations of the device's fluid dynamic properties, for instance, carried out with finite element analysis (FEA) tools, provide valuable insights for the careful design of flow devices [90]. An example is presented in figure 4, which shows three different configurations of the inlet and outlet ports (while keeping the dimensions and volume of the flow chamber constant). The motion of the liquid electrolyte was simulated using COMSOL software to solve the Navier-Stokes equations (conservation of momentum) and the continuity equation (conservation of mass), with the boundary conditions imposed by the three selected configurations. Liquid velocity fields are depicted for three different flow rates (1, 5, and 10 ml min^{-1}). Noteworthy, no stagnant electrolyte regions (i.e. the velocity of the fluid equal to zero) on the working electrode surface are observed for configuration 2 compared to configurations 1 and 3, likely due to the overall lower fluid velocity that allows a more homogeneous circulation of the liquid in the flow chamber. Additionally, configuration 2 provides better flow homogeneity across the working electrode surface than the other configurations for flow rates of 5 and 10 ml min^{-1}. Configurations 1 and 3 generate, for the same flow rates, tight jet streams that hinder a homogeneous distribution of the liquid electrolyte over the working electrode surface. Thus, geometry 2 was chosen for the configuration of the liquid inlet/outlet of the *in situ/operando* PEC flow cell, which is detailed in the 'State of the art of *operando* RS of semiconducting photoelectrodes and devices for photoelectrochemistry' section.

- Optical transparency: the cell components, particularly the windows or transparent electrodes through which light

J. Phys. D: Appl. Phys. **57** (2024) 103002

Topical Review

enters the cell, should possess high optical transparency over the desired spectral range. This ensures that a significant fraction of incident light can reach the photoactive electrode and generate photocurrent or drive PEC reactions. Selecting materials with low absorption and high transmittance is crucial for accurately characterizing the photoelectrode's performance.

- Electrical contact: proper electrical contact between the photoactive electrode and external circuitry is essential for accurately measuring the PEC response. The cell design should incorporate robust electrical connections to ensure low resistance pathways and minimize contact potential drops. This allows for precise measurement of the photocurrent and photovoltage-related observables, such as the half-cell open circuit potential, generated by the photoelectrode.

- Gas management: the PEC cell and the overall setup design should facilitate efficient gas management if the PEC processes involve gas evolution or consumption. This includes provisions for gas supply, collection, and separation, as well as the removal of gas bubbles from the electrolyte flow. As mentioned above, adequate gas management prevents gas bubble accumulation at the electrode surface, which can impede PEC reactions, increase kinetic overpotentials, limit light absorption, or cause uncontrolled system performance variations [89].

- Temperature control: temperature has a significant influence on PEC processes, affecting reaction rates, charge carrier mobility, charge transfer kinetics, and material stability. Therefore, a flow PEC cell should incorporate temperature control mechanisms. This may involve a temperature-controlled bath or a Peltier-based cooling/heating system to maintain the desired operating temperature. Additionally, the electrolyte temperature should be monitored in different locations of the liquid circuit to allow the quantification of eventual heat losses. Precise temperature control allows for systematic investigations and accurate comparison of results under different conditions.

- Stability and leak prevention: the cell design should be robust and leak-proof to ensure consistent and reliable operation. Sealing of the cell components, such as O-rings or gaskets, should be chosen carefully to withstand the corrosive nature of the electrolyte and avoid unwanted leakage that can compromise experimental results and safety.

- Versatility and modularity: a well-designed flow PEC cell should allow for easy modifications and adaptability to accommodate different electrode materials, catalysts, and experimental configurations (such as electrode size scale-up or operations with pressurized liquid electrolytes). This versatility enables systematic studies and comparisons between various systems, facilitating the advancement of PEC research.

- Ability to implement *in situ/operando* characterization tools: PEC systems involve complex interfaces between the semiconductor electrode, electrolyte, and eventual co-catalysts. The ability to interface complementary *in situ/operando* characterization tools in the same flow device enables the characterization of these interfaces during the electrochemical and PEC processes [91]. For instance, RS

can be used for real-time monitoring of structural changes and phase transitions in active materials during PEC reactions. RS can also reveal vibrational signatures of reaction intermediates and identify specific reaction products in the electrolyte. These combined capabilities are essential for understanding the mechanisms and kinetics of PEC reactions, gaining valuable information on the materials' degradation mechanisms, and, consequently, designing strategies to enhance the stability and lifetime of PEC flow devices. RS can be effectively used together with electron spectroscopies (e.g. x-ray photoelectron spectroscopy, XPS, and x-ray absorption spectroscopy, XAS), the latter primarily providing information about the electronic structure, chemical composition, and local bonding in materials [92]. Hence, the combination of *operando* RS with electron spectroscopies in PEC flow devices provides a means to establish correlations between structural/electronic properties and chemical composition of the materials involved and to explore their combined effects on the overall device performance. This knowledge is crucial for rational materials design and optimization, facilitating the development of more efficient PEC materials and devices.

Considering these characteristics, a flow PEC cell can provide meaningful and reproducible results, enabling accurate characterization and optimization of photoelectrodes for various applications and light-driven reactions. A practical example of such a flow PEC device is reported below in the section 'State of the art of *operando* RS of semiconducting photoelectrodes and devices for photoelectrochemistry.'

7. State of the art of *operando* RS of semiconducting photoelectrodes and devices for photoelectrochemistry

Operando RS for investigating semiconducting photoelectrodes and devices for photoelectrochemistry has not been applied yet to many scientific cases. All these (few) studies share a common experimental approach, named in this perspective as the 'continuous irradiation method': an external laser with a wavelength lower than that used to induce and detect the Raman scattering is used to promote free charge carriers in the photoabsorbers under investigation. As the name suggests, in this approach, the irradiation by the external laser is kept constant throughout the experiment. Similarly to what has been described above for photocatalysis investigations, the RS can be performed using a higher wavelength laser, acquiring the Stokes lines, and using a high-pass (long wave pass, LWP) edge filter in front of the detector to eliminate the spectral component of the excitation laser from the multiplexed signal. Note that the notch/LWP filters installed in any Raman setup dedicated to the detection of the Stokes lines and used to suppress the Rayleigh line can also serve this purpose, depending on the specifications of the particular optical analysis system in use. Adopting this approach, Ramakrishnan and co-workers recently investigated the role of hole-trapping surface states in hematite photoanodes as reaction intermediates
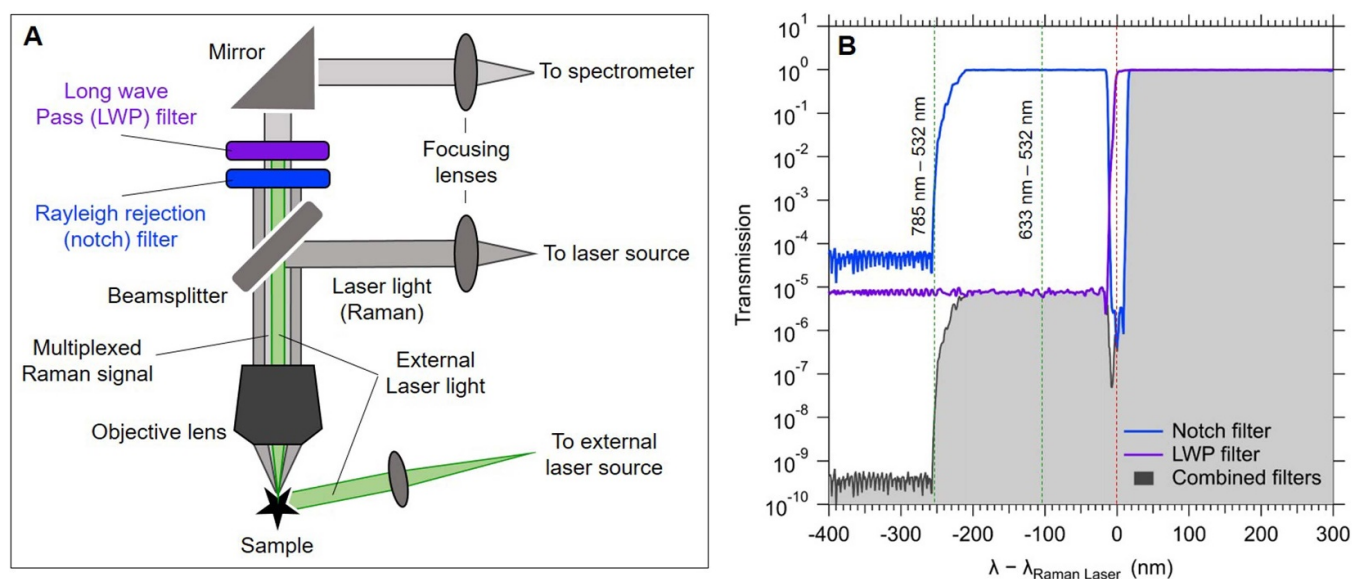
Figure 5. (A) Schematic of the continuous irradiation principle for *in situ/operando* RS using an external laser source to excite semiconducting light absorbers. (B) optical transmission for a typical notch/long wave pass (LWP) filter system placed in front of the monochromator/detector in the Raman setup. Note that the wavelength of the laser used to detect the Raman signal is set at 0 nm to extend the discussion's general validity. The combined transmission of the two optical filters in series was determined by convolving the transmission of the individual filters since the light influences the output of one filter passed through the previous filter.

using sacrificial reducing compounds such as H_2O_2 and FeCN as hole scavengers [54]. Using *operando* RS coupled with a PEC investigation of the system above, the authors observed a competitive photo-oxidation between H_2O_2, FeCN, and water at low scavenger concentrations and intermediate potentials. Such competition leads to non-linear behavior and hysteresis in photocurrent voltammograms. Steady-state and transient *operando* RS confirmed that the detected transient spectral features were associated with both the scavenger adsorption and the involvement of surface species in the photo-oxidation of the hole scavenger and water [54]. These findings represent a promising application of *operando* RS to the field of photo-electrochemistry, particularly enhancing the understanding of the role of surface species in water splitting and contributing to the optimization of hematite photoelectrode performance. For their investigations, the authors used a confocal micro-Raman system equipped with a light source of 633 nm (red laser), operating at a total spectral power of 12 mW. Given the energy band gap of hematite ($\sim$1.8–2.2 eV), an external 532 nm laser ($\sim$2.3 eV) was used as an excitation source, set to a power density of $\sim$100 mW cm^{-2} at the sample surface to simulate the sunlight power. Figure 5(A) reports a schematic of the described continuous irradiation method, while the optical transmission for a typical notch/LWP filter system used for Raman applications is shown in figure 5(B). As observed, any external laser with a wavelength at least 50 nm below that used to induce and collect the Raman signal can be adopted without perturbing the detection since the transmitted fraction eventually reaching the detector is less than 10 ppm, at most. This is well-documented by the wavelength shift ($\Delta\lambda$) for an external 532 nm laser with respect to 633 nm ($\Delta\lambda = 101$ nm) and 785 nm ($\Delta\lambda = 253$ nm), two standard wavelengths used to induce and detect the Raman signal.

Similarly, in the author's laboratory blue (450 nm) and green (532 nm) lasers are available to perform *in situ/operando* RS of wide band gap ($\sim$1.8–2.5 eV) light absorbers under continuous irradiation, using a 785 nm laser to detect the Raman signal. It is important to highlight that the working principle described above for the continuous irradiation method is only valid for Raman setups detecting the Stokes lines. Systems allowing the possibility to detect the Anti-Stokes lines are not equipped with LWP filters since the scattered light is analyzed for energies above and below the excitation. Hence, only the notch edge filter is present to remove the excitation line that would saturate the detector selectively. However, most Raman setups allow detecting the Stokes lines since they are characterized by a higher intensity compared to Anti-Stokes lines at room temperature, as described in the 'Principles and theory of RS' section.

It is important to note that benchmarking PEC investigations are performed using broadband light sources (bias lights) that mimic the solar spectrum (e.g. *AM*1.5 illumination conditions) regarding spectral components and corresponding intensities. In addition, it is well-reported in the literature that light of different wavelengths can impact on the selectivity of light-driven chemical reactions [93–97]. For reactions involving homogeneous co-catalysts and more complex mechanisms than water splitting, such as biomass reforming, which include various intermediates and products, the use of a single, selected wavelength to excite charge carriers in the photoelectrode may yield different outcomes compared to conducting the same experiment under broadband light conditions resembling *AM*1.5. Moreover, when tandem or multi-junction photoelectrode systems are used, multiple materials with different bandgaps (and therefore different absorption cut offs) are integrated into a single device [98, 99]. This setup enables
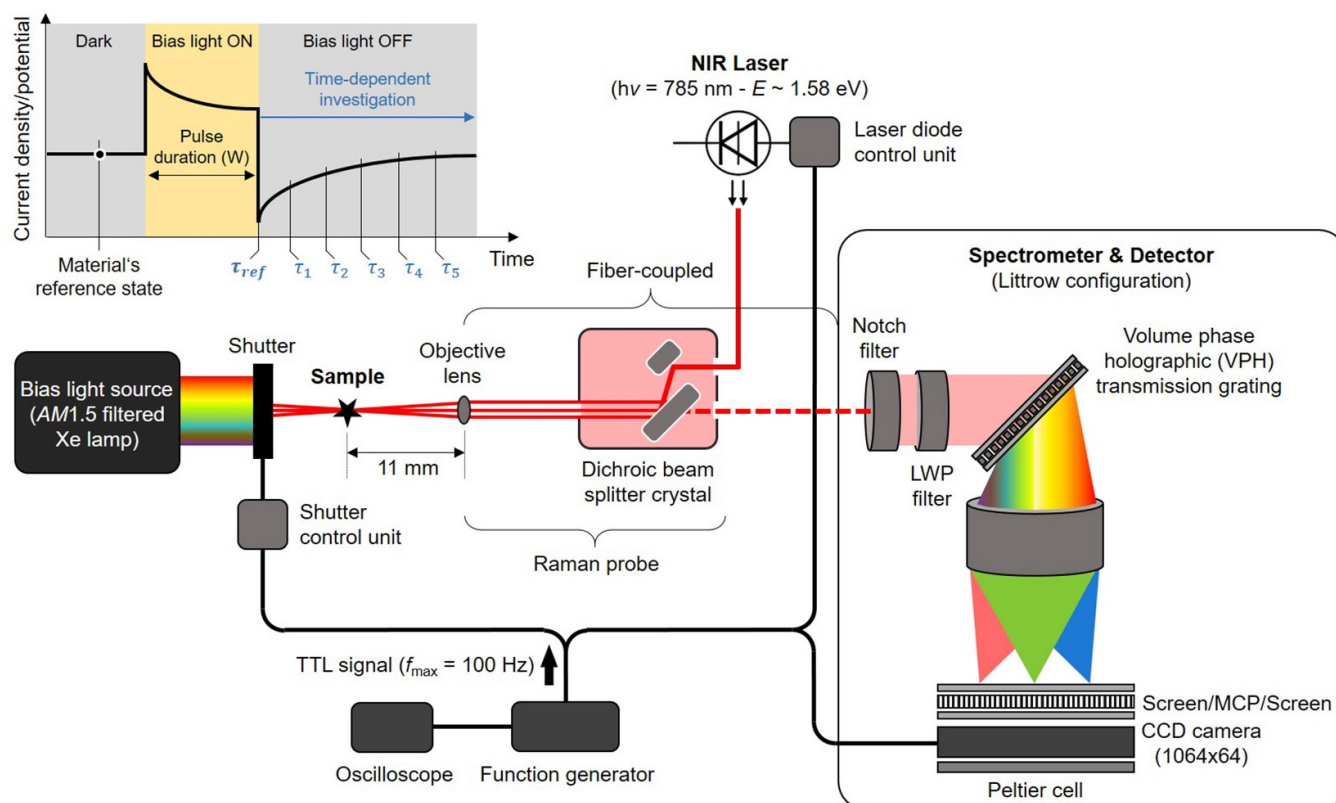
J. Phys. D: Appl. Phys. **57** (2024) 103002

Topical Review

Figure 6. Schematic diagram of the fiber-coupled RS setup developed at the Institute for Solar Fuels at the Helmholtz-Zentrum Berlin. The setup is built around the Wasatch Photonics WP 785 ER spectrometer.

the sequential absorption of light at various wavelengths, promoting efficient charge separation and utilization of the entire solar spectrum. Hence, *in situ/operando* RS investigations would greatly benefit from closely resembling the illumination conditions used in PEC devices, since it will enable the investigation of complex sample architectures and a broader portfolio of light-driven chemical reactions. The disadvantage of using a broadband light source in combination with RS is the spectral overlap existing between the frequencies of the bias light and the scattered laser light, making *operando* RS challenging to perform under actual PEC conditions (*AM*1.5). A possible solution, enabled by an experimental configuration developed at the Institute for Solar Fuels of the Helmholtz Zentrum Berlin and schematically reported in figure 6, is to detect the Raman spectra in 'dark' conditions (to avoid the aforementioned spectral overlap) immediately after a 'pulse' of bias light directed to the sample. The investigation of the spectral differences existing between the time-dependent spectra taken after the bias light pulse and those taken before the pulse of bias light (i.e. the 'reference state' of the investigated material) allows detecting possible transient material instabilities (i.e. photocorrosion), the presence of reaction intermediates/products adsorbed on the photoelectrode, or local changes in the pH at the semiconductor/liquid electrolyte interface due to the ongoing reaction [100].

Transient Raman spectra are obtained by synchronously triggering the bias light shutter (tuning the pulse duration), the laser diode, the RS setup's laser diode, and the CCD detector. The triggering signal, fed to the transistor-transistor-logic

(TTL) gate of the components mentioned above, is an analogic sinusoidal voltage signal with an amplitude of 5 V produced by a function generator. The electronic chain is set up in a way that the reference for the time base (i.e. the 'time zero' τ_{ref}) of the Raman spectra detection is when the shutter closes. The statistics of the measurements (i.e. signal-to-noise ratio on the detected signals) can be increased by taking the average over multiple repeated cycles. By tuning the duration of the bias light pulse W (i.e. by changing the frequency of the triggering signal) and the time delay along the time-dependent polarization curve of the photoelectrode (see schematic reported in figure 6), it is possible to gain information on the relaxation/degradation mechanisms occurring at the semiconductor/liquid electrolyte interface for time scales spanning from 10 ms (100 Hz) up to hours. Additionally, working in the range of tens to hundreds of milliseconds, real-time monitoring of chemical reactions occurring at the photoelectrode surface under investigation can be enabled.

In addition to the detection stage of the Raman signal, a coupled multimodal *in situ/operando* device has been recently developed at the Institute for Solar Fuels. Figure 7 reports a schematic process flow diagram (PFD) for such a device. Here, photoelectrodes are investigated in a dedicated and fully customized PEC cell. The liquid electrolyte is circulated by an 8-rotor peristaltic pump, providing low pulsation even at relatively high flow rates (typical flow rates range between 0.5 ml min^{-1} and 50 ml min^{-1}). A fluid capacitor/liquid mixer is inserted in the circuit after the pump to dampen any pulsation, providing a continuous and stable flow stream.
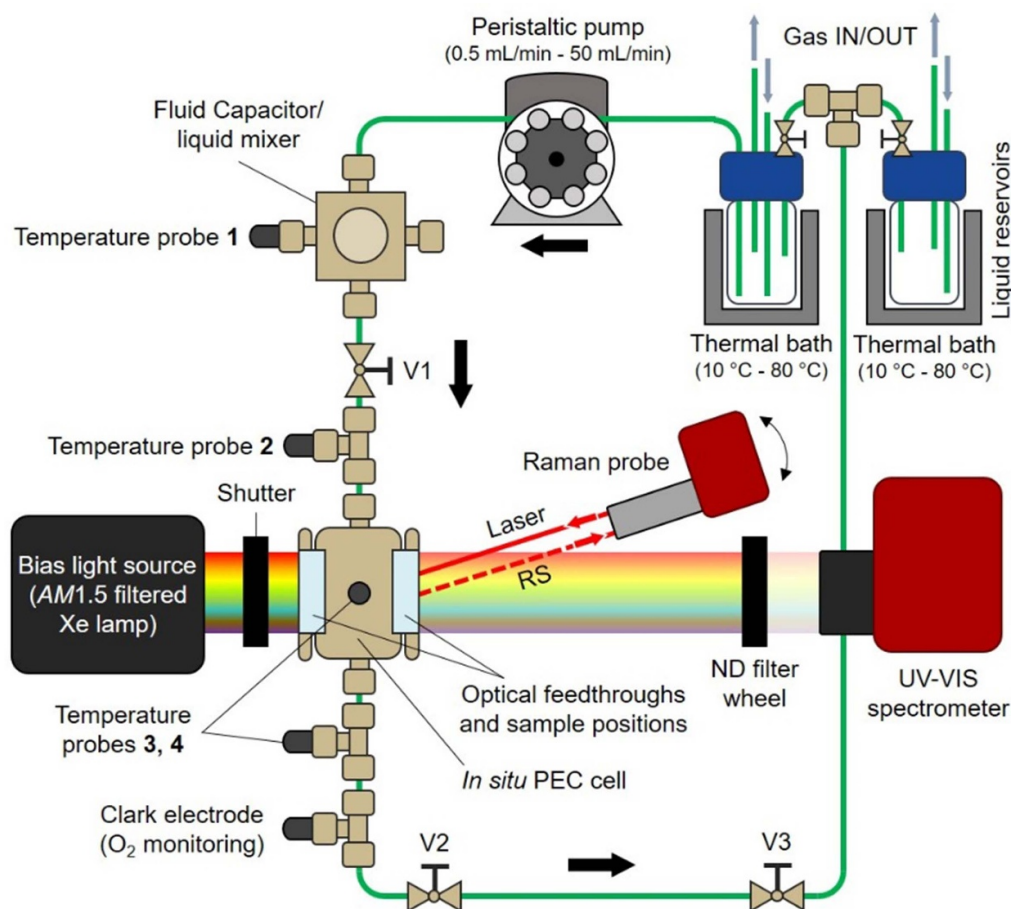
Figure 7. Schematic process flow diagram (PFD) diagram of the *in situ/operando* Raman spectroscopy setup developed at the Institute for Solar Fuels at the Helmholtz-Zentrum Berlin. The figure shows that the sample under investigation can be placed on either optical window, equipping the photoelectrochemical (PEC) cell.

Next, the liquid enters the customized PEC cell, as detailed in figures 8(A)–(F). The single-compartment cell can operate in a two- or three-electrode configuration. Even when used in a three-electrode configuration, the cell voltage ($\Delta E_{WE–CE}$) is monitored and logged by a 6 1/2 digit digital multimeter connected to the sample (working electrode) and the counter electrode. To minimize the load on the circuit during the measurements (i.e. current flowing between the two electrodes), the input resistance of the multimeter is set between 10 MΩ and 10 GΩ, depending on the cell voltage values and currents achieved during the measurements (note that for an input resistance of 1 GΩ and a cell voltage of about 2 V, a typical value in PEC measurements, the 'leakage' current will be about 2 nA. With respect to a photocurrent of few mA, as showed in figure 3(a), the leakage current is therefore below 1 ppm). The cell is provided with two quartz optical feedthroughs to enable front or back illumination of the photoelectrodes, additionally allowing the coupling of different optical spectroscopies as described below. Immediately after the cell, a miniaturized Clark electrode detects the amount of oxygen in the liquid stream, thus allowing the real-time determination of the solar-to-hydrogen efficiency. The electrolyte can flow back to the same feeding reservoir, enabling recirculation of the liquid, or it can be collected on an independent vessel. The electrolyte reservoirs can be cooled and heated in a temperature range of 10 °C–80 °C to perform electrokinetic studies. As reported in figure 7, the electrolyte temperature is monitored at four different locations along the liquid circuit using local probes (figure 8(G)): at the fluid capacitor downstream of the peristaltic pump, before the PEC cell, within the PEC cell, and immediately after it. These four temperature values are automatically logged throughout the investigations. PEC measurements are performed using an *AM*1.5 filtered Xe lamp. During illumination, a high-performance UV–VIS spectrometer operating in the 200–1000 nm range allows for performing *in situ/operando* optical transmittance analysis (OTA) of the transmitted light fraction through the photoelectrode. OTA enables observing the evolution of the sample's transmittance as a function of light intensity/time/current density/ flow patterns, thereby providing valuable information on the stability and degradation mechanisms of the investigated photoelectrodes. Finally, *in situ/operando* time-resolved RS can be performed as described above.

As a proof of concept measurement, figure 9 demonstrates an *operando* RS performed with the experimental setup and working principle described above, where a paradigmatic photoanode (bismuth vanadate, BiVO$_4$) was investigated under PEC conditions with a time resolution of 100 ms, without

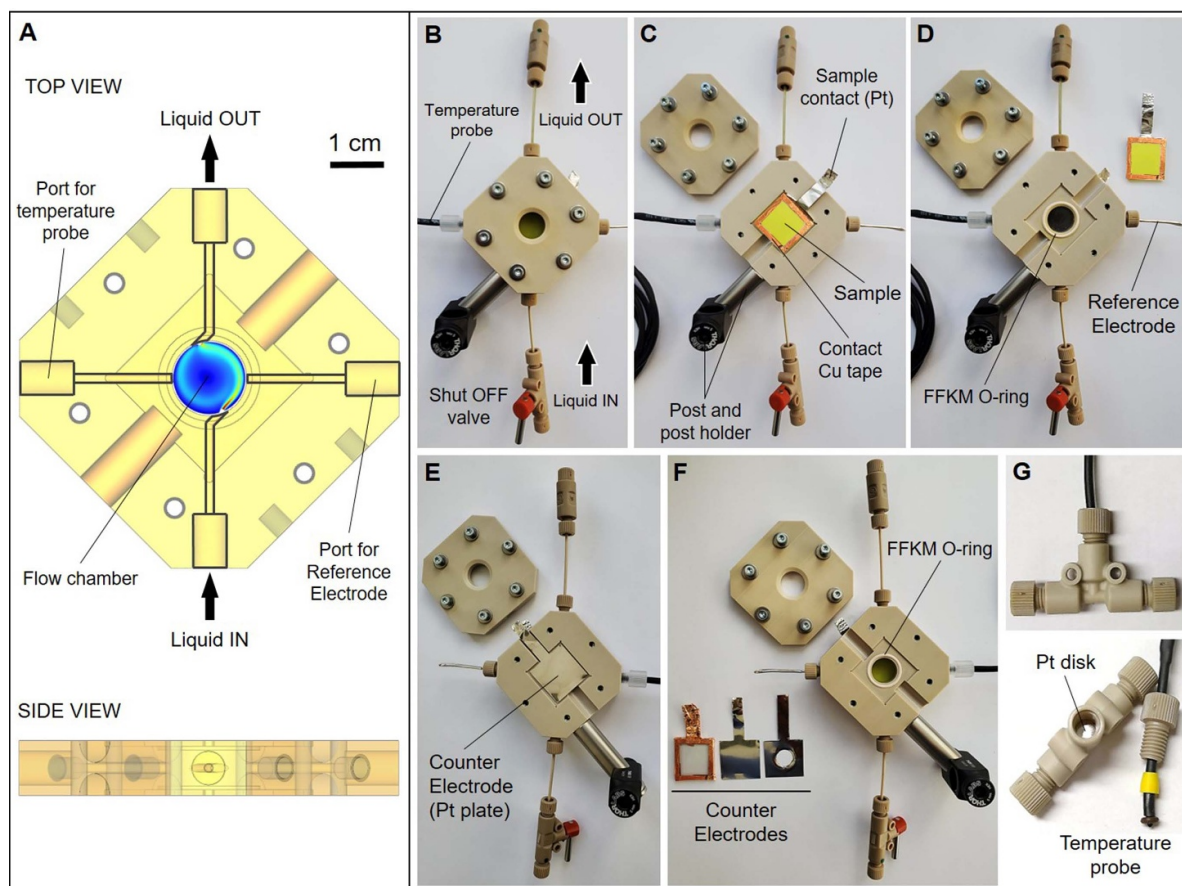J. Phys. D: Appl. Phys. **57** (2024) 103002

Topical Review

Figure 8. (A) Semi-transparent 3D rendering of the multipurpose *in situ/operando* PEC cell, highlighting the inlet and outlet ports and the ports for hosting the reference electrode and the probe for cell temperature monitoring. The velocity field obtained for a flow rate of 10 ml min^{-1} is superimposed to the rendering to show the electrolyte motion inside the cell. (B)–(D) Digital photographs of the cell, sample (working electrode) side. This side is oriented toward the simulated sunlight for *back illumination* investigations. (E), (F) Digital photographs of the cell, counter electrode (CE) side. Different CEs are compatible with the cell, allowing the possibility to direct the simulated sunlight from the CE side (*front illumination* measurements). (G) Temperature probe structure monitoring the temperature of the liquid electrolyte in different circuit locations.

sacrificing the S/N ratio. A single crystalline Mo:BiVO$_4$(010) (Mo doping ∼1 at.% [101]) was placed in contact with an aqueous solution containing 0.5 mol l^{-1} of potassium phosphate (KPi, used as a buffering supporting electrolyte) and 0.1 mol l^{-1} of glycerol as a hole scavenger. The flow rate was kept constant at 10 ml min^{-1}. A Pt wire and a miniaturized Ag/AgCl/Cl$^-$$_{KCl\,3.5M}$ electrode were used as counter and reference electrodes, respectively. The Raman spectrum of the photoanode immersed in the aqueous electrolyte, shown in figure 9(A) (trace a), was taken at the half-cell open circuit potential in dark conditions (i.e. no bias light). Figure 9(A) also reports the different spectral references taken during the experiment, namely the Raman spectrum of a pristine single crystalline Mo:BiVO$_4$(010) prior to the exposure to the solution (trace b), the Raman spectrum of the aqueous solution containing 0.5 mol l^{-1} of KPi and 0.1 mol l^{-1} of glycerol (trace c), the Raman spectrum of an aqueous solution containing 0.1 mol l^{-1} of glycerol (trace d), and the Raman spectrum of pure glycerol (trace e). Figure 9(B) reports the time-resolved *operando* Raman spectra taken on the system mentioned above after subtracting the spectral contribution due to the liquid

electrolyte (i.e. trace a—trace c for the indicated time delays). If no changes occur in the electrolyte, as in this reported example, such different spectra can be used to highlight better the time dependency of the sample's spectral features, thereby identifying time-dependent responses of the photoabsorber under investigation. To allow a better comparison, note that the intensity of the spectra reported in figure 9(B) was normalized to the highest intensity band, i.e. the V–O symmetric stretching mode band (*vide infra*). The measurements were performed at the half-cell open circuit potential after a pulse of bias light of 10 s, recording the Raman spectra for 1 s after closing the shutter. The spectra were taken continuously with an integration time of 100 ms, thereby obtaining ten spectra with an increasing delay time from the first spectrum of the series. Note that the laser wavelength was 785 nm, and the power was set to 300 mW. The Raman spectrum of Mo:BiVO$_4$(010) exhibits three distinct spectral features. The lowest energy band, centered at 345.5 cm^{-1}, is attributed to the symmetric and anti-symmetric bending modes (δ_{as} and δ_s) of the vanadate anion (VO$_4^{3-}$) [64]. Typically, these two modes are reported well separated in energy, centered
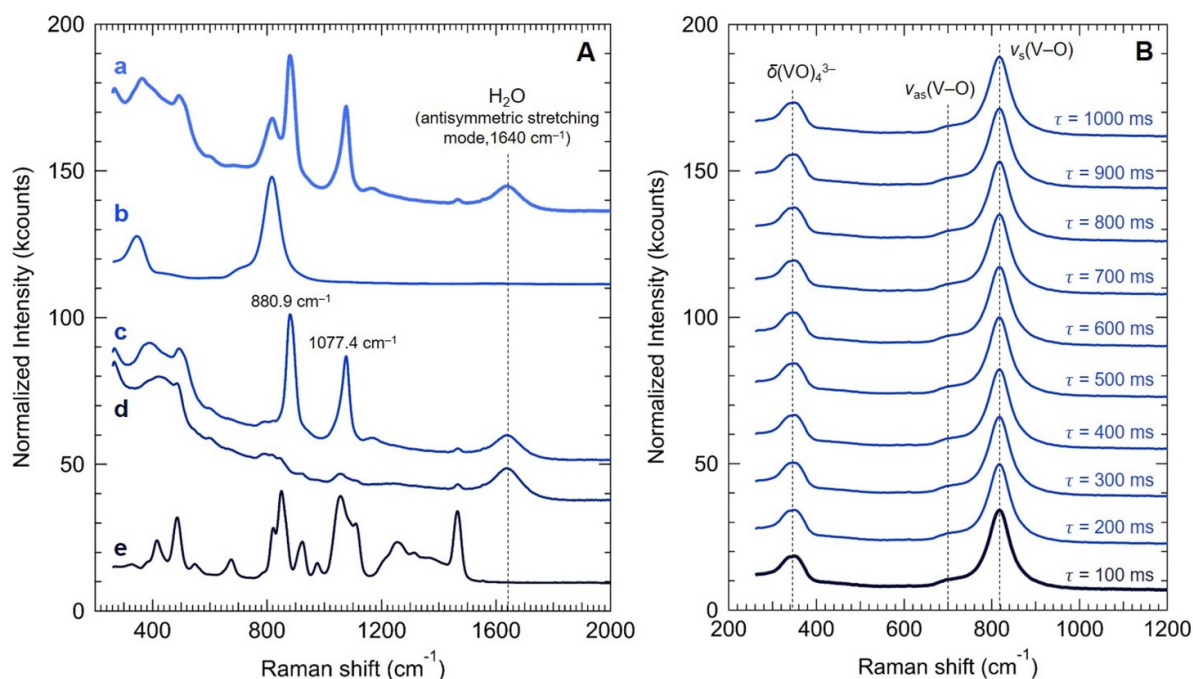
Figure 9. (A) Raman spectra of different samples taken with the experimental configuration described in the text at room temperature (22 °C). Trace a: single crystalline Mo:BiVO$_4$(010) in contact with an aqueous solution containing 0.5 mol l^{-1} of potassium phosphate (KPi) and 0.1 mol l^{-1} of glycerol as a hole scavenger. The Raman spectrum was taken at the half-cell open circuit potential in dark before the pulse of bias light (i.e. the material's reference state); Trace b: Raman spectrum of a pristine single crystalline Mo:BiVO$_4$(010) prior to the exposure to the solution; Trace c: Raman spectrum of the aqueous solution containing 0.5 mol l^{-1} of KPi and 0.1 mol l^{-1} of glycerol; Trace d: Raman spectrum of an aqueous solution containing 0.1 mol l^{-1} of glycerol; Trace e: Raman spectrum of pure glycerol. The investigation of the solutions was conducted in dedicated quartz cuvettes. The energy axis was calibrated using the 520 cm^{-1} mode of Si. (B) Time-resolved *operando* Raman spectra obtained after subtracting the spectral contribution of the liquid electrolyte. The measurements were performed at the half-cell open circuit potential after a pulse of bias light of 10 s, recording the Raman spectra for 1 s after closing the shutter. The spectra were taken continuously with an integration time of 100 ms, thereby obtaining ten spectra with an increasing delay time from the first spectrum of the series. The laser wavelength was 785 nm, and the power was 300 mW. For a better comparison, the intensity of the spectra was normalized to the highest intensity band (V–O symmetric stretching mode at 816.3 cm^{-1}) and reported with a vertical offset.

at about 321 cm^{-1} and 363 cm^{-1}, respectively [64]. In our case, we can observe that the band is characterized by a relatively high spectral broadening (full width at half maximum, FWHM, about 55 cm^{-1}); although both modes are likely present, the energy resolution of our setup does not allow to detect them as individual bands. At higher energy, we observe the two modes generated by the antisymmetric (ν_{as}) and symmetric (ν_s) stretching of the V–O bond, centered at about 700 cm^{-1} and 816.3, respectively. We note that both modes are centered at slightly lower wavenumbers compared to the values reported in the literature (see table 1 and [64]). As shown by the spectra reported in figure 9(B), the photoelectrode immersed in the solution was stable after the exposure to the bias light, exhibiting no evident changes (i.e. shift or broadening) of the spectral bands described above with respect to trace b. These findings conclude that no photocorrosion was present on the timescales explored during this experiment.

Finally, the system and its operating principle described in this paragraph allow the detection of the *operando* PL of semiconductors with energy band gaps smaller than 1.58 eV (this being the energy of the laser used to induce the

Raman scattering and/or PL in the investigated materials). Figure 10(A) reports the PL detected at the half-cell open circuit potential for three different III–V semiconductors in contact with an aqueous solution containing 0.5 mol l^{-1} of KPi as a supporting electrolyte. The flow rate was kept constant at 10 ml min^{-1}. A Pt wire and a miniaturized Ag/AgCl/Cl$^-_{KCl\,3.5M}$ electrode were used as counter and reference electrodes, respectively. The PL was detected 10 ms after a pulse of bias light of 10 s. The integration time was 10 ms, and the laser power was 50 mW. The PL obtained from n-doped Si (n-Si(110)) under the same conditions is reported as a reference. As proof of the capabilities of the setup, figure 10(B) reports the time-resolved *operando* PL spectra of InP/n-Si(110). The data were recorded for 100 ms after a pulse of bias light of 10 s with an integration time of 10 ms, thereby obtaining ten spectra with an increasing delay time from the first spectrum of the series. This capability can be used to observe transient changes in the electronic structure, particularly in the energy band gap of the investigated photoabsorbers as a function of the explored experimental conditions (light exposure and intensity, temperature and nature of the electrolyte, etc).
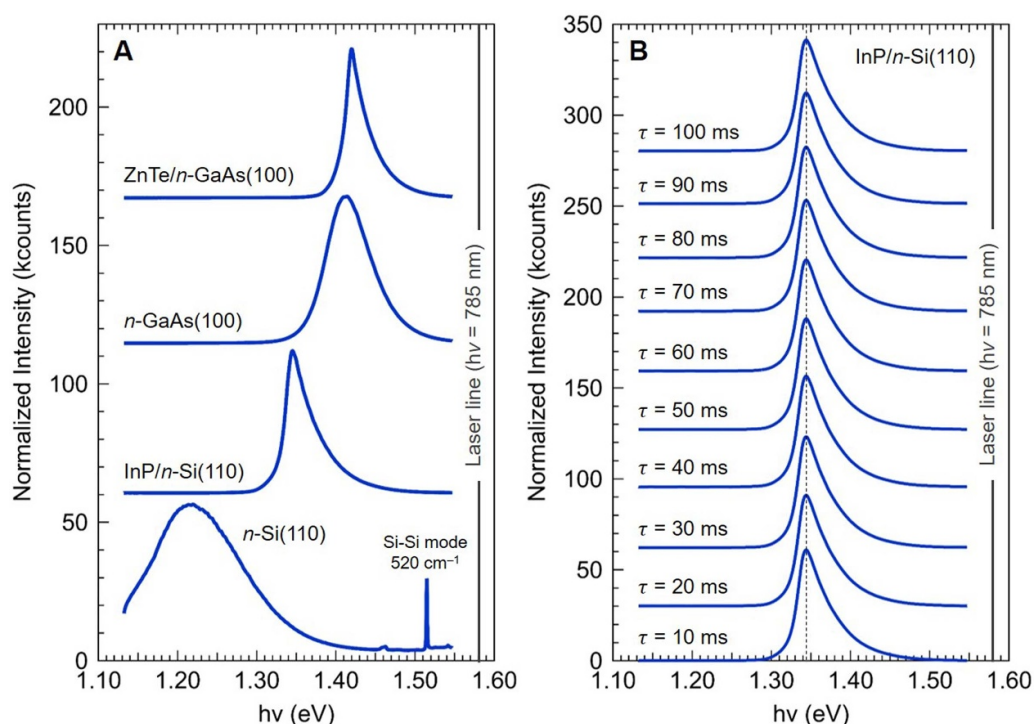
Figure 10. (A) Example of *operando* photoluminescence (PL) measurements of narrow band gap semiconductors ($E_g < 1.5$ eV), detected at room temperature (22 °C) with the setup and working principle described in the text. The PL was detected using a laser wavelength of 785 nm (∼1.58 eV), with the power set to 50 mW. The spectra were acquired at the half-cell open circuit potential with the semiconductors in contact with an aqueous solution containing 0.5 mol l^{-1} of KPi as a supporting electrolyte. The flow rate was kept constant at 10 ml min^{-1}. (A) PL spectra of *n*-Si(110) (taken as reference), InP/*n*-Si(110), *n*-GaAs(100, and ZnTe/*n*-GaAs(100), detected 10 ms after a pulse of bias light of 10 s with an integration time of 10 ms. (B) Time-resolved *operando* PL spectra of InP/*n*-Si(110), taken after a pulse of bias light of 10 s. The spectra were continuously recorded for 100 ms after closing the shutter with an integration time of 10 ms, thereby obtaining ten spectra with an increasing delay time from the first spectrum of the series. Note that for both figures (A) and (B), the spectra have been normalized to the maximum PL intensity and reported with a vertical offset for a better comparison.

8. Conclusion and future perspective

RS can be applied under various *in situ* and *operando* conditions. However, its use and implementation are still underdeveloped in the study and the characterization of semiconducting photoelectrodes and devices for photoelectrochemistry. With the development in recent years of versatile, compact, all-in-one Raman spectrometers, material scientists have more flexibility in designing experimental setups to investigate novel material systems and reactions. Our analysis examined the challenges in applying *operando* RS to PEC reactions, encompassing potential limitations such as the limited quantum efficiency of inelastic scattering and fluorescence. We reviewed standard signal enhancement techniques that can improve sensitivity, such as SERS or resonance Raman scattering. An essential aspect of performing meaningful *in situ/operando* analysis of PEC processes is the reactor geometry prerequisites and the environmental conditions surrounding the photoelectrode sample. We showed that using FEA can direct the reactor optimization via the simulation of the fluid dynamics at the photoelectrode surface to obtain homogeneous liquid flows that can maximize the mass transport and, in turn, the performance of the reactor. With such an optimized cell configuration, we showed that

RS could be employed to analyze the liquid stream leaving the PEC cell when other reactions, such as the reduction or oxidation of organic substrates, substitute the usual water-splitting reaction. Conducting quantitative analysis with RS can be challenging due to the inherent low intensity of the Raman signal and the eventual spectral overlap between the reactants and products. This requires a case-by-case evaluation that considers the scattering power of the molecules involved in the process and the concentration of the products. Advanced analysis methods such as PLS, arPLS, or IHM can be used to mitigate these challenges. However, we want to highlight that product analysis performed with RS should always be benchmarked against other analytical techniques, such as nuclear magnetic resonance spectroscopy and high-performance liquid chromatography. Finally, we described a new methodology for performing *operando* RS with illumination resembling *AM*1.5 conditions. The time resolution spans from tens to hundreds of milliseconds, suitable timescales for real-time monitoring of chemical reactions and degradation mechanisms occurring at the photoelectrode under investigation. We showcased the possibility of investigating a photoelectrode surface in a working environment subjected to cycles of dark and illumination conditions without compromising on the *S/N* ratio of the measurements. Future applications of this

method will encompass pulsing the bias light with different frequencies and shapes of the pulse train while holding constant the potential or current at the photoelectrode.

RS offers insights into the molecular vibrations, crystal structure, and composition of materials. It can be used to probe changes in the lattice structure, the presence of impurities or defects, and surface species. PEC techniques involve measuring various parameters, such as photocurrent, open-circuit voltage, kinetic overpotentials, and electrochemical impedance, to evaluate the performance and stability of PEC devices. These techniques provide insights into the device's charge transport mechanisms, interfacial processes, and reaction kinetics. Hence, combining these techniques in synergy can comprehensively understand the relationship between the chemical composition, surface electronic states, crystal structure and degree of crystallinity, and PEC performance. Therefore, rational multimodal *operando* investigations will help identify key factors influencing PEC devices' efficiency, selectivity, and stability and their relationship with synthesis pathways and crystallographic structure. For instance, x-ray photoelectron and absorption spectroscopy (XPS, XAS) provide valuable insights into materials' electronic properties and chemical composition. XPS can identify the elemental composition and chemical/oxidation state of the surface species and the energetics of a semiconductor surface in terms of Fermi level, work function, and valence band maximum. XAS provides information on the local electronic and structural environment. Examining the electronic states at the solid/liquid interface using x-ray spectroscopies makes it possible to understand the charge transfer processes, surface reactions, and redox reactions occurring during PEC reactions. This can be efficiently combined with RS. Such knowledge can then be exploited to develop new, improved materials and device designs to minimize photovoltage losses and optimize charge carrier extraction. Both are essential requirements for the practical deployment and scale-up of PEC energy conversion devices.

Data availability statement

All data that support the findings of this study are included within the article (and any supplementary files).

Acknowledgments

Author contributions

Both authors contributed equally to the conceptualization and the writing of the manuscript. HK prepared the polycrystalline $BiVO_4$ samples and performed the photoelectrochemical investigations.

Conflict of interest

The authors declare no competing interests.

ORCID iDs

Marco Favaro ⓘ https://orcid.org/0000-0002-3502-8332
Heejung Kong ⓘ https://orcid.org/0000-0001-8009-7292
Ronen Gottesman ⓘ https://orcid.org/0000-0001-5223-478X

References

[1] Walter M G, Warren E L, McKone J R, Boettcher S W, Mi Q, Santori E A and Lewis N S 2010 Solar water splitting cells *Chem. Rev.* **110** 6446–73

[2] van de Krol R and Parkinson B A 2017 Perspectives on the photoelectrochemical storage of solar energy *MRS Energy Sustain.* A **4** E13

[3] Kumaravel V, Bartlett J and Pillai S C 2020 Photoelectrochemical conversion of carbon dioxide (CO_2) into fuels and value-added products *ACS Energy Lett.* **2020** 486–519

[4] Zhang W, Jin Z and Chen Z 2022 Rational-designed principles for electrochemical and photoelectrochemical upgrading of CO_2 to value-added chemicals *Adv. Sci.* **9** 1–30

[5] Verma S and Yadav A 2023 Emerging single-atom catalysts and nanomaterials for photoelectrochemical reduction of carbon dioxide to value-added products: a review of the current state-of-the-art and future perspectives *Energy Fuels* **37** 5712–42

[6] Fujishima A and Honda K 1972 Electrochemical photolysis of water at a semiconductor electrode *Nature* **238** 37–38

[7] Sivula K and van de Krol R 2016 Semiconducting materials for photoelectrochemical energy conversion *Nat. Rev. Mater.* **1** 15010

[8] Yao T, An X, Han H, Chen J Q and Li C 2018 Photoelectrocatalytic materials for solar water splitting *Adv. Energy Mater.* **8** 1–36

[9] Chen Z *et al* 2010 Accelerating materials development for photoelectrochemical hydrogen production: standards for methods, definitions, and reporting protocols *J. Mater. Res.* **25** 3–16

[10] Morikawa T, Sato S, Sekizawa K, Suzuki T M and Arai T 2022 Solar-driven CO_2 reduction using a semiconductor/molecule hybrid photosystem: from photocatalysts to a monolithic artificial leaf *Acc. Chem. Res.* **55** 933–43

J. Phys. D: Appl. Phys. **57** (2024) 103002

Topical Review

[11] Nielander A C, Shaner M R, Papadantonakis K M, Francis S A and Lewis N S 2015 A taxonomy for solar fuels generators *Energy Environ. Sci.* **8** 16–25

[12] Singh A K, Zhou L, Shinde A, Suram S K, Montoya J H, Gregoire J M and Persson K A 2017 Electrochemical stability of metastable materials *Chem. Mater.* **29** 10159–67

[13] Sun W *et al* 2019 A map of the inorganic ternary metal nitrides *Nat. Mater.* **18** 732–9

[14] van de Krol R 2020 A faster path to solar water splitting *Matter* **3** 1389–91

[15] Maeda K and Domen K 2010 Photocatalytic water splitting: recent progress and future challenges *J. Phys. Chem. Lett.* **1** 2655–61

[16] Segev G *et al* 2022 The 2022 solar fuels roadmap *J. Phys. D: Appl. Phys.* **55** 323003

[17] Gottesman R, Levine I, Schleuning M, Irani R, Abou-ras D, Dittrich T, Friedrich D and van de Krol R 2021 Overcoming phase-purity challenges in complex metal oxide photoelectrodes: a case study of $CuBi_2O_4$ *Adv. Energy Mater.* **11** 2003474

[18] Gottesman R, Peracchi I, Gerke J, Irani R, Abdi F F and van de Krol R 2022 Shining a hot light on emerging photoabsorber materials: the power of rapid radiative heating in developing oxide thin-film photoelectrodes *ACS Energy Lett.* **7** 514–22

[19] Schleuning M, Kölbach M, Abdi F F, Schwarzburg K, Stolterfoht M, Eichberger R, van de Krol R, Friedrich D and Hempel H 2022 Generalized method to extract carrier diffusion length from photoconductivity transients: cases of $BiVO_4$, halide perovskites, and amorphous and crystalline silicon *PRX Energy* **1** 023008

[20] Kay A, Fiegenbaum-Raz M, Müller S, Eichberger R, Dotan H, van de Krol R, Abdi F F, Rothschild A, Friedrich D and Grave D A 2019 Effect of doping and excitation wavelength on charge carrier dynamics in hematite by time-resolved microwave and terahertz photoconductivity *Adv. Funct. Mater.* **30** 1901590

[21] Schleuning M *et al* 2023 Carrier localization on the nanometer-scale limits transport in metal oxide photoabsorbers *Adv. Funct. Mater.* **33** 2300065

[22] Chase D B 1986 Fourier transform Raman spectroscopy *J. Am. Chem. Soc.* **108** 7485–8

[23] McCreery R L 2001, *Raman Spectroscopy for Chemical Analysis* vol 12 (Wiley)

[24] Esmonde-White K A, Cuellar M, Uerpmann C, Lenain B and Lewis I R 2017 Raman spectroscopy as a process analytical technology for pharmaceutical manufacturing and bioprocessing *Anal. Bioanal. Chem.* **409** 637–49

[25] Nagy B, Farkas A, Borbás E, Vass P, Nagy Z K and Marosi G 2019 Raman spectroscopy for process analytical technologies of pharmaceutical secondary manufacturing *AAPS PharmSciTech* **20** 1–16

[26] Rantanen J 2010 Process analytical applications of Raman spectroscopy *J. Pharm. Pharmacol.* **59** 171–7

[27] Doty K C, Muro C K, Bueno J, Halámková L and Lednev I K 2016 What can Raman spectroscopy do for criminalistics? *J. Raman Spectrosc.* **47** 39–50

[28] Neuville D R, de Ligny D and Henderson G S 2014 Advances in Raman spectroscopy applied to earth and material sciences *Spectrosc. Methods Mineral. Mater. Sci.* **78** 509–41

[29] Chakrabarti A *et al* 2017 A decade+ of operando spectroscopy studies *Catal. Today* **283** 27–53

[30] Mu C, Lv C, Meng X, Sun J, Tong Z and Huang K 2023 *In situ* characterization techniques applied in photocatalysis: a review *Adv. Mater. Interfaces* **10** 2201842

[31] Baddour-Hadjean R and Pereira-Ramos J P 2010 Raman microspectrometry applied to the study of electrode materials for lithium batteries *AIP Conf. Proc.* **1267** 1137–8

[32] Zheng Y, Deng T, Yue N, Zhang W, Zhu X, Yang H, Chu X and Zheng W 2021 Raman spectroscopy and correlative-Raman technology excel as an optimal stage for carbon-based electrode materials in electrochemical energy storage *J. Raman Spectrosc.* **52** 2119–30

[33] Bañares M A 2005 Operando methodology: combination of *in situ* spectroscopy and simultaneous activity measurements under catalytic reaction conditions *Catal. Today* **100** 71–77

[34] Portela R, Perez-Ferreras S, Serrano-Lotina A and Bañares M A 2018 Engineering operando methodology: understanding catalysis in time and space *Front. Chem. Sci. Eng.* **12** 509–36

[35] Mestl G 2000 *In situ* Raman spectroscopy—a valuable tool to understand operating catalysts *J. Mol. Catal.* A **158** 45–65

[36] Bell S E J 1996 Tutorial review. Time-resolved resonance Raman spectroscopy *Analyst* **121** 107R–20R

[37] Reichert P, Kjær K S, Brandt Van Driel T, Mars J, Ochsmann J W, Pontoni D, Deutsch M, Nielsen M M and Mezger M 2018 Molecular scale structure and dynamics at an ionic liquid/electrode interface *Faraday Discuss.* **206** 141–57

[38] Dery S, Friedman B, Shema H and Gross E 2023 Mechanistic insights gained by high spatial resolution reactivity mapping of homogeneous and heterogeneous (Electro)catalysts *Chem. Rev.* **123** 6003–38

[39] Aarnoutse P J and Westerhuis J A 2005 Quantitative Raman reaction monitoring using the solvent as internal standard *Anal. Chem.* **77** 1228–36

[40] AlSalka Y, Schwabe S, Geweke J, Ctistis G and Wackerbarth H 2023 Electrochemical and photoelectrochemical water splitting: operando Raman and Fourier transform infrared spectroscopy as useful probing techniques *Energy Technol.* **11** 1–21

[41] Liu Y and Guo L 2020 On factors limiting the performance of photoelectrochemical CO_2 reduction *J. Chem. Phys.* **152** 100901

[42] Hess C 2013 *In situ* Raman spectroscopy of catalysts: examples from current research *Top. Catal.* **56** 1593–600

[43] Hanlon E B, Manoharan R, Koo T W, Shafer K E, Motz J T, Fitzmaurice M, Kramer J R, Itzkan I, Dasari R R and Feld M S 2000 Prospects for *in vivo* Raman spectroscopy *Phys. Med. Biol.* **45** R1–59

[44] Damle V H, Gouda L, Tirosh S and Tischler Y R 2018 Structural characterization and room temperature low-frequency Raman scattering from $MAPbI_3$ halide perovskite films rigidized by cesium incorporation *ACS Appl. Energy Mater.* **1** 6707–13

[45] Yang W, Prabhakar R R, Tan J, Tilley S D and Moon J 2019 Strategies for enhancing the photocurrent, photovoltage, and stability of photoelectrodes for photoelectrochemical water splitting *Chem. Soc. Rev.* **48** 4979–5015

[46] Glass D, Quesada-Cabrera R, Bardey S, Promdet P, Sapienza R, Keller V, Maier S A, Caps V, Parkin I P and Cortés E 2021 Probing the role of atomic defects in photocatalytic systems through photoinduced enhanced Raman scattering *ACS Energy Lett.* **6** 4273–81

[47] Mandal L *et al* 2018 Investigating the role of copper oxide in electrochemical CO_2 reduction in real time *ACS Appl. Mater. Interfaces* **10** 8574–84

[48] Drake M C and Rosenblatt G M 1976 Flame temperatures from Raman scattering *Chem. Phys. Lett.* **44** 313–6

[49] Brites C D S, Lima P P, Silva N J O, Millán A, Amaral V S, Palacio F and Carlos L D 2012 Thermometry at the nanoscale *Nanoscale* **4** 4799–829

[50] Maher R C, Cohen L F, Gallop J C, Le Ru E C and Etchegoin P G 2006 Temperature-dependent

J. Phys. D: Appl. Phys. **57** (2024) 103002

Topical Review

anti-Stokes/Stokes ratios under surface-enhanced Raman scattering conditions *J. Phys. Chem.* B **110** 6797–803

[51] Xie X and Cahill D G 2016 Thermometry of plasmonic nanostructures by anti-S tokes electronic Raman scattering *Appl. Phys. Lett.* **109**

[52] Chua Y T and Stair P C 2000 A novel fluidized bed technique for measuring UV Raman spectra of catalysts and adsorbates *J. Catal.* **196** 66–72

[53] Schleuning M, Ahmet I Y, van de Krol R and May M M 2022 The role of selective contacts and built-in field for charge separation and transport in photoelectrochemical devices *Sustain. Energy Fuels* **6** 3701–16

[54] Ramakrishnan V, Tsyganok A, Davydova E, Pavan M J, Rothschild A and Visoly-fisher I 2023 Competitive photo-oxidation of water and hole scavengers on hematite photoanodes: photoelectrochemical and operando Raman spectroelectrochemistry study *ACS Catal.* **13** 540–9

[55] Mao Z, Ye Y, Lv H, Han X X, Park Y, Zang L, Zhao B and Jung Y M 2020 Direct dynamic evidence of charge separation in a dye-sensitized solar cell obtained under operando conditions by Raman spectroscopy *Angew. Chem., Int. Ed.* **59** 10780–4

[56] Qi Y, Hu D, Jiang Y, Wu Z, Zheng M, Chen E X, Liang Y, Sadi M A, Zhang K and Chen Y P 2023 Recent progresses in machine learning assisted Raman spectroscopy *Adv. Opt. Mater.* **11** 2203104

[57] Fan X, Ming W, Zeng H, Zhang Z and Lu H 2019 Deep learning-based component identification for the Raman spectra of mixtures *Analyst* **144** 1789–98

[58] Smith E and Dent G 2019 *Modern Raman Spectroscopy: A Practical Approach* (Wiley) (https://doi.org/10.1002/9781119440598)

[59] Ferraro J R, Nakamoto K and Brown C W 2003 *Introductory Raman Spectroscopy* (Elsevier Science)

[60] Raman C V 1928 A new radiation *Indian J. Phys.* **2** 387–98

[61] Raman C V and Krishnan K S 1928 A new type of secondary radiation *Nature* **121** 501–2

[62] Senthilkumar R, Ravi G, Sekar C, Arivanandhan M, Navaneethan M and Hayakawa Y 2015 Determination of gas sensing properties of thermally evaporated WO_3 nanostructures *J. Mater. Sci.: Mater. Electron.* **26** 1389–94

[63] Szatkowski T *et al* 2015 Novel nanostructured hematite–spongin composite developed using an extreme biomimetic approach *RSC Adv.* **5** 79031–40

[64] Tsay C Y, Chung C Y, Chen C Y, Chang Y C, Chang C J and Wu J J 2023 Enhanced photocatalytic performance of visible-light-driven $BiVO_4$ nanoparticles through W and Mo substituting *Catalysts* **13** 475

[65] Davies J E D 1973 Solid state vibrational spectroscopy—III[1] The infrared and raman spectra of the bismuth(III) oxide halides *J. Inorg. Nucl. Chem.* **35** 1531–4

[66] Geraldes C F G C 2020 Introduction to infrared and Raman-based biomedical molecular imaging and comparison with other modalities *Molecules* **25** 5547

[67] Langer J *et al* 2020 Present and future of surface-enhanced Raman scattering *ACS Nano* **14** 28–117

[68] Shan F, Zhang X Y, Fu X C, Zhang L J, Su D, Wang S J, Wu J Y and Zhang T 2017 Investigation of simultaneously existed Raman scattering enhancement and inhibiting fluorescence using surface modified gold nanostars as SERS probes *Sci. Rep.* **7** 1–10

[69] Lipiäinen T *et al* 2018 Time-gated Raman spectroscopy for quantitative determination of solid-state forms of fluorescent pharmaceuticals *Anal. Chem.* **90** 4832–9

[70] Kögler M and Heilala B 2021 Time-gated Raman spectroscopy—a review *Meas. Sci. Technol.* **32** 012002

[71] Reid P J, Lawless M K, Wickham S D and Mathies R A 1994 Determination of pericyclic photochemical reaction dynamics with resonance Raman spectroscopy *J. Phys. Chem.* **98** 5597–606

[72] Heck K N, Janesko B G, Scuseria G E, Halas N J and Wong M S 2008 Observing metal-catalyzed chemical reactions *in situ* using surface-enhanced Raman spectroscopy on Pd-Au nanoshells *J. Am. Chem. Soc.* **130** 16592–600

[73] Schmitt M 2014 Analysis of silanes and of siloxanes formation by Raman spectroscopy *RSC Adv.* **4** 1907–17

[74] Meher A K and Chen Y C 2016 Combination of Raman spectroscopy and mass spectrometry for online chemical analysis *Anal. Chem.* **88** 9151–7

[75] Šahnić D, Meštrović E, Jednačak T, Habinovec I, Parlov Vuković J and Novak P 2016 Monitoring and quantification of omeprazole synthesis reaction by in-line Raman spectroscopy and characterization of the reaction components *Org. Process Res. Dev.* **20** 2092–9

[76] McDonald K J and Choi K S 2012 A new electrochemical synthesis route for a BiOI electrode and its conversion to a highly efficient porous $BiVO_4$ photoanode for solar water oxidation *Energy Environ. Sci.* **5** 8553–7

[77] Garcia-Navarro J, Isaacs M A, Favaro M, Ren D, Ong W J, Grätzel M and Jiménez-Calvo P 2023 Updates on hydrogen value chain: a strategic roadmap *Glob. Challenges* **2300073** 1–17

[78] Luo H, Barrio J, Sunny N, Li A, Steier L, Shah N, Stephens I E L and Titirici M M 2021 Progress and perspectives in photo- and electrochemical-oxidation of biomass for sustainable chemicals and hydrogen production *Adv. Energy Mater.* **11** 2101180

[79] Lin J A, Roh I and Yang P 2023 Photochemical diodes for simultaneous bias-free glycerol valorization and hydrogen evolution *J. Am. Chem. Soc.* **145** 12987–91

[80] Han X, Sheng H, Yu C, Walker T W, Huber G W, Qiu J and Jin S 2020 Electrocatalytic oxidation of glycerol to formic acid by $CuCo_2O_4$ spinel oxide nanostructure catalysts *ACS Catal.* **10** 6741–52

[81] Pakrieva E, Kolobova E, German D, Stucchi M, Villa A, Prati L, Carabineiro S A C, Bogdanchikova N, Corberán V C and Pestryakov A 2020 Glycerol oxidation over supported gold catalysts: the combined effect of au particle size and basicity of support *Processes* **8** 1016

[82] Qiao Z, Wang Z, Zhang C, Yuan S, Zhu Y and Wang J 2012 PVAm–PIP/PS composite membrane with high performance for CO_2/N_2 separation *AIChE J.* **59** 215–28

[83] Baek S-J, Park A, Ahn Y-J and Choo J 2015 Baseline correction using asymmetrically reweighted penalized least squares smoothing *Analyst* **140** 250–7

[84] Kriesten E, Mayer D, Alsmeyer F, Minnich C B, Greiner L and Marquardt W 2008 Identification of unknown pure component spectra by indirect hard modeling *Chemom. Intell. Lab. Syst.* **93** 108–19

[85] Beumers P, Engel D, Brands T, Koß H J and Bardow A 2018 Robust analysis of spectra with strong background signals by first-derivative indirect hard modeling (FD-IHM) *Chemom. Intell. Lab. Syst.* **172** 1–9

[86] S-PACT GmbH PEAXACT Products 2023 (available at: www.s-pact.de/en/peaxact-software-products) (Accessed 2 December 2023)

[87] Modestino M A, Hashemi S M H and Haussener S 2016 Mass transport aspects of electrochemical solar-hydrogen generation *Energy Environ. Sci.* **9** 1533–51

[88] Davis J T and Esposito D V 2017 Limiting photocurrent analysis of a wide channel photoelectrochemical flow reactor *J. Phys. D: Appl. Phys.* **50** aa5538

J. Phys. D: Appl. Phys. **57** (2024) 103002

Topical Review

[89] Holmes-Gentle I, Bedoya-Lora F, Alhersh F and Hellgardt K 2019 Optical losses at gas evolving photoelectrodes: implications for photoelectrochemical water splitting *J. Phys. Chem.* C **123** 17–28

[90] Stender F J, Obata K, Baumung M, Abdi F F and Risch M 2023 A modular double electrode flow cell with exchangeable generator and detector electrodes *ChemElectroChem* **10** e202300126

[91] Yalavarthi R, Henrotte O, Minguzzi A, Ghigna P, Grave D A and Naldoni A 2020 *In situ* characterizations of photoelectrochemical cells for solar fuels and chemicals *MRS Energy Sustain.* **7** 1–27

[92] Lewerenz H J *et al* 2016 Operando analyses of solar fuels light absorbers and catalysts *Electrochim. Acta* **211** 711–9

[93] Haas C P, Roider T, Hoffmann R W and Tallarek U 2019 Light as a reaction parameter-systematic wavelength screening in photochemical synthesis *React. Chem. Eng.* **4** 1912–6

[94] Protti S, Ravelli D and Fagnoni M 2019 Wavelength dependence and wavelength selectivity in photochemical reactions *Photochem. Photobiol. Sci.* **18** 2094–101

[95] Menzel J P, Noble B B, Blinco J P and Barner-Kowollik C 2021 Predicting wavelength-dependent photochemical reactivity and selectivity *Nat. Commun.* **12** 1–12

[96] Markushyna Y and Savateev A 2022 Light as a tool in organic photocatalysis: multi-photon excitation and chromoselective reactions *Eur. J. Org. Chem.* **2022** e202200026

[97] Lunic D, Bergamaschi E and Teskey C J 2021 Using light to modify the selectivity of transition metal catalysed transformations *Angew. Chem.* **133** 20762–73

[98] Prévot M S and Sivula K 2013 Photoelectrochemical tandem cells for solar water splitting *J. Phys. Chem.* C **117** 17879–93

[99] Chen Y, Feng X, Liu Y, Guan X, Burda C and Guo L 2020 Metal oxide-based tandem cells for self-biased photoelectrochemical water splitting metal oxide-based tandem cells for self-biased photoelectrochemical water splitting *ACS Energy Lett.* **5** 844–66

[100] Lackey H E, Nelson G L, Lines A M and Bryan S A 2020 Reimagining pH measurement: utilizing Raman spectroscopy for enhanced accuracy in phosphoric acid systems *Anal. Chem.* **92** 5882–9

[101] Favaro M, Uecker R, Nappini S, Píš I, Magnano E, Bluhm H, van de Krol R and Starr D E 2019 Chemical, structural and electronic characterization of the (010) surface of single crystalline bismuth vanadate *J. Phys. Chem.* C **123** 8347–59